Charge carrier dynamics and photoelectrochemical properties of photocatalyst single crystals for solar-to-hydrogen energy conversion

（太陽-水素エネルギー変換用光触媒単結晶の電荷キャリアダイナミクスと光電気化学特性）

ZHANG Endong

Thesis submitted in partial fulfilment of the requirements for the award of the Doctoral (PhD) Degree of Engineering

Department of Electrical and Mechanical Engineering

Graduate School of Engineering

Nagoya Institute of Technology

Nagoya

Japan

March 2024

Charge carrier dynamics and photoelectrochemical properties of photocatalyst single crystals for solar-to-hydrogen energy conversion

（太陽-水素エネルギー変換用光触媒単結晶の電荷キャリアダイナミクスと光電気化学特性）

Acknowledgments

First, I would like to express my heartfelt gratitude to my advisor, Prof. Masashi Kato, for providing invaluable guidance and advice throughout my doctoral research. Not only did my supervisor offer patience and direction in academic matters, but also showed unwavering care and support in personal aspects throughout the entire journey.

I would also like to extend my thanks to Prof. Tsukasa Torimoto from Nagoya University, Prof. Naoki Kishi from Nagoya Insititute of Technology, and Prof. Christoph J. Brabec from Friedrich-Alexander Universität Erlangen-Nürnberg, who, despite a busy schedule, provided valuable insights and suggestions for my doctoral thesis. Their expertise and unique perspectives in the research field played a crucial role in advancing my doctoral studies.

Throughout the entire research process, I received tremendous support from colleagues, Mr. Takuto Maeda, Mr. Toshiki Mii, Mr. Lei Han, Mr. Tong Li, Mr. Mingxin Zhang, Mr. Kongshik Rho, Ms. Ntumba Lobo, and Mr. Kazuhiro Tanaka. Their team spirit created an excellent environment for my research work.

A special acknowledgment goes to my family who have been my pillars of strength throughout my entire doctoral journey. Their understanding, support, and encouragement have been the driving force behind my continuous progress.

Lastly, I want to express my gratitude to the JGGE program for providing an opportunity to have a half-year research stay at FAU in Germany. This valuable experience provided significant help in academic and personal aspects and the exchange of different cultures.

Thanks to everyone who contributed to my doctoral studies, your efforts will be indelible memories on my life's journey.

Abstract

In recent years, hydrogen has been expected as a clean alternative energy source to fossil fuels in addressing environmental degradation and energy shortage problems. There are various methods that have been developed to generate hydrogen. Among them, solar-to-hydrogen (STH) energy conversion has been attracting attention only by using inexhaustible solar energy and water without CO_2 production. Using photocatalysts, hydrogen can be produced by photoelectrochemical (PEC) water splitting from renewable energy.

Charge carrier dynamics refers to the motion and behavior of excited electrons or holes in a material. Herein, among numerous properties of charge carrier dynamics, the carrier lifetime (carrier recombination) of photocatalysts is mainly characterized because it can directly affect the PEC performance of photocatalysts, especially the STH energy conversion efficiency. Therefore, the carrier lifetime becomes particularly important for photocatalysts.

There are six chapters in this thesis. In the first chapter, the background on hydrogen energy and conventional hydrogen production methods are briefly introduced. Furthermore, the advantages of solar-to-hydrogen, photocatalyst, the advantage of single crystal, and charge carrier dynamics are also explained. Afterward, the basic properties of TiO_2, 3C-SiC, $BiVO_4$, $SrTiO_3$, and CeO_2 which are utilized in this work, are also introduced.

In the second chapter, a tandem structure combined with n-type TiO_2 and p-type 3C-SiC exhibits an efficient and durable solar water-splitting system. It is observed that the photocurrent from the tandem structure is higher at low pH, as noted by the pH dependence of the photocurrent at the TiO_2 photoanode. The photocurrent from the tandem structure has a light intensity dependence similar to the photocurrent from the TiO_2 photoanode. Therefore, the performance of the tandem structure appears to be

limited by the photocurrents from the TiO$_2$ photoanode. We obtain a maximum applied bias photon-to-current (ABPE) conversion efficiency of approximately 0.74% from the tandem structure with no additional bias applied. We also confirm the presence of a stable photocurrent from the tandem structure for over ~100 days.

In the third chapter, we characterize the carrier lifetime in BiVO$_4$ single crystals on the (100) and (001) crystal faces using the microwave photoconductivity decay (μ-PCD) method. For the (001) face, the observed μ-PCD curves with excitation by a 266 nm laser have no injected photon density dependence. In contrast, those excited using a 355 nm laser show injected photon density dependence. For the (100) face, the decay curves at both excitations of 266 and 355 nm are not significantly different, and they depend on the injected photon density. These results indicate that the carrier lifetime is dominated by surface recombination only under the 266 nm excitation condition for the (001) face, whereas under other conditions, this is dominated by the Schokley-Read-Hall (SRH) recombination. We estimate the surface recombination velocities and bulk lifetimes of the samples by fitting the experimental results into the calculations.

In the fourth chapter, we analyze the effect of dislocations on carrier recombination in TiO$_2$ and SrTiO$_3$ using the μ-PCD method on polished and unpolished faces. The apparent slow decay in the unpolished face implies that dislocations trap minority carriers. Based on the different dependences of the injected photon density and temperature, the recombination processes in the polished and unpolished faces differ. A high concentration of oxygen vacancies in the unpolished face of SrTiO$_3$ is observed by X-ray photoelectron spectroscopy (XPS), and dislocations in the unpolished faces of both materials are observed using transmission electron microscopy (TEM). Additionally, we ind that the photocurrent duration in the unpolished faces is shorter than that in the polished faces for both TiO$_2$ and SrTiO$_3$, confirming that dislocations inhibit photoelectrochemical activity.

In the fifth chapter, we analyze the defects that can directly dominate carrier recombination for the photocatalytic performance of CeO_2. Several photoluminescence (PL) peaks are observed on the (100) face of an undoped CeO_2 single crystal, indicating the presence of defects. Moreover, we characterize its carrier recombination using time-resolved photoluminescence (TR-PL) and μ-PCD methods. The temperature dependence of the decay curves is the result of carrier trapping and emission at deep levels. These decay curves are observed separately using a 565 nm band-pass filter (BPF) based on the PL spectra. The trap energy level E_t and electron capture cross-section σ_n of each defect are also analyzed using rate equations to fit the experimental results.

Finally, in the sixth chapter, the conclusion and future work outlook are presented.

Table of contents

Chapter 1

Introduction

1.1 Hydrogen energy

In recent years, with the exacerbation of global warming and the deterioration of the environment, coupled with the escalating issue of energy shortages, hydrogen has received widespread attention as a more promising and widely applicable clean energy source.

1.1.1 Conventional production methods

1.1.1.1 Steam Methane Reforming (SMR)

SMR is a typical industrial hydrogen production method [1–3]. Hydrocarbon compounds, such as natural gas (CH_4) and petroleum, are utilized to react with water vapor (H_2O) at high temperatures to produce syngas, which are then converted to hydrogen by a water gas conversion reaction. However, carbon monoxide (CO) is one of the by-products of chemical reactions. CO is a toxic gas that can be very harmful to the human body. Therefore, this method is not suitable for building a clean energy system with hydrogen.

1.1.1.2 Partial Oxidation of Hydrocarbons (POX)

POX is another common production method [4–6]. Different from the SMR method, the hydrocarbon compounds reacted with a limited amount of oxygen to produce hydrogen, carbon monoxide, and some amount of carbon dioxide (CO_2). The dangers of CO have already been mentioned above. However, the generated CO_2 is a greenhouse gas that, if produced in large quantities, can accelerate global warming. Therefore, it is difficult to produce large-scale hydrogen using this method.

1

1.1.1.3 Coal Gasification

Coal gasification [7,8] is the process of converting coal into syngas at high temperatures and in an oxygen-poor (or partially oxygen-poor) environment, with the syngas consisting mainly of CO, H_2, CH_4, CO_2, and so on. The proportion of hydrogen in the syngas is pretty low; thus, most of them are greenhouse gases. Therefore, similar to SMR and POX, these methods based on carbon or hydrocarbon compounds are not friendly to the environment.

1.1.2 Water splitting

Hydrogen can be obtained not only from fossil fuels but also through water splitting. Water splitting is the cleanest method to produce hydrogen because it is a process that breaks water into hydrogen and oxygen (O_2) gases. Without CO_2 emission, it has recently attracted attention and has been widely studied so far.

1.1.2.1 Electrolysis of water (electricity-to-hydrogen)

Electrolysis of water has a long history around 230 years since the first observation in 1789 [9]. From 1799, with the invention of connecting a plurality of electrochemical cells together to produce a battery with a relatively high voltage by Alessandro Volta, the technology of electrolysis of water is continuously being developed [10,11].

Electrolysis of water is considered to be an efficient and scalable method of achieving this electricity-to-hydrogen conversion, producing hydrogen and oxygen with just an input of water and electricity [12]. Therefore, it is a clean and echo friendly method to produce hydrogen and can be considered to be widely adopted.

Several types of water electrolysis, including alkaline water electrolysis [13–16], polymer electrolyte membrane (PEM) water electrolysis [17–20], and high-temperature water electrolysis [21–24]. With its long history and various types, electrolysis has become a mature technology, however, electricity is a secondary energy source that

should be converted by the primary energy source, such as solar energy, tidal, and nuclear energy. Therefore, there will be energy loss during the production process, especially the thermal energy.

1.1.2.2 Photolysis of water (solar-to-hydrogen)

Photolysis of water is a promising and novel method for hydrogen production. In 1972, Fujishima and Honda [25] reported the use of a rutile-type TiO_2 photoanode for photoelectrochemical (PEC) water splitting which is also called the Honda-Fujishima effect. Subsequently, numerous studies on the water splitting of semiconductor materials have been initiated.

The energy difference between the oxygen oxidation potential and the hydrogen reduction potential is 1.23 eV at room temperature (RT). Consequently, for this reaction to take place, it is advantageous to employ a chemically stable semiconductor with conduction and valence bands positioned favorably to straddle the hydrogen and oxygen evolution potentials [24,26,27].

When a semiconductor is irradiated with solar energy higher than its band gap, electrons in the valence band are excited to the conduction band, and holes are created in the valence band. If the potential of the valence band is higher than the oxidation potential of water, the holes oxidize water to produce oxygen, and if the potential of the conduction band is lower than the reduction potential of water, water is reduced by electrons to produce hydrogen [28,29]. In other words, if the band gap of a semiconductor is located across the redox potential of water, the semiconductor has the potential to complete water splitting.

Photolysis of water becomes particularly intriguing that by employing only semiconductors and solar energy, one can produce both hydrogen and oxygen. With the use of primary solar energy source and water from nature, if this method can be widely applied, it will be a great contribution to addressing energy and environmental issues.

1.1.2.3 Three-electrode system

The three-electrode system [12] is generally used in both electrolysis and photolysis of water. The working electrode is where the actual electrochemical reaction takes place. The counter electrode is an electrode used to balance the flow of current in an electrochemical cell. It provides a site for current reactions to keep the current balance. The reference electrode is an electrode with a known potential that is relatively stable and is used as a reference point for potentials in electrochemical experiments. The most commonly used reference electrodes are saturated calomel electrode (SCE) [30–32], standard hydrogen electrode (SHE) [33,34], reversible hydrogen electrode (RHE) [35], and Ag/AgCl electrode [36–38] in water-splitting experiments.

1.1.2.4 Two-electrode system

The two-electrode system [39,40] is another common system in the electrolysis and photolysis of water. However, different from the three-electrode system, it consists of only a working electrode and a counter electrode, the reference electrode is not used. This difference also leads to different applications from the three-electrode system. One of the applications is that using a two-electrode system can simulate the actual water-splitting process.

In the photolysis of water, this two-electrode system is also called the tandem structure in this work. In traditional water photolysis structures, the absorption capacities of different materials for various wavelengths of light differ. As a result, light cannot be fully absorbed, leading to a reduction in the efficiency of solar energy utilization. However, in a tandem structure, different photoelectrodes are placed in series, in this way, the solar energy transmitted from the photoelectrode will be absorbed by another photoelectrode. This greatly improves the utilization of solar energy avoiding energy waste. In addition, only using solar energy and tandem structure without the bias applied, a simple self-driving cell can be made for water photolysis.

1.2 Photocatalyst

Photocatalyst, generally, refers to those materials that absorb light and then promote the chemical reaction [41–45]. Due to this property, it can be applied in various fields, such as wastewater treatment [20,44,46], organic synthesis promotion [47–49], fuel cell [50–52], CO_2 reduction [53,54]. Furthermore, photocatalytic water splitting [27,29,55] is mainly discussed in this work.

There are various crystal structures developed for improving the performance of photocatalysts. Generally, large-size structures should be investigated to characterize photocatalytic performance. However, in order to improve the STH energy conversion efficiency, micrometer-size [56,57] and nano-scale [58,59] structures are being widely investigated due to the large contact area with the aqueous solutions. Moreover, powder and film are developed for the improvement of high-efficiency photocatalytic CO_2 reduction and water splitting [60,61]. Recently, the quantum dots photocatalyst [62] has been created due to the great advantage of excellent visible light absorption, multi-exciton effect, surface effect, and adjustable energy bands. However, using these structures, the most essential factors affecting conversion efficiency such as defect, and surface status, could not be clearly realized.

1.2.1 Advantages of single crystal

In this work, we mainly investigate the single crystal structure. With the advantage of structural ordering, the defect and crystal lattice are uniform so that we can clearly realize the effect of defect, or crystalline quality on photocatalytic activity. Moreover, the crystal face can be precisely controlled, so we can also study the effect of surface status on each crystal face on the photocatalytic performance [63]. Hence better controllability of catalytically active sites and selective exposure of crystalline surfaces with high catalytic activity. Additionally, single-crystal materials can be designed to specific sizes and shapes, thereby tuning their optical and electronic properties. This tunability is valuable for manufacturing photocatalysts to satisfy the requirements of

different reactions. Finally, generally, using a large-scale material, we can also simply test the long-term durability and stability which are the most important properties for the wide applications of photocatalysts [34].

1.3 Charge carrier dynamics

Charge carrier dynamics is the movement and behavior of excited carriers, i.e., electrons and holes in a material. To realize the charge carrier dynamics sufficiently, we can study on several concepts, such as carrier recombination, carrier lifetime, carrier concentration, band structure, impact of defect, and drift and diffusion. In this work, we mainly focus on the carrier recombination and carrier lifetime.

1.3.1 Carrier recombination and carrier lifetime

Carrier recombination is a process of carriers from excitation to recombination. When excess carriers are injected by some factor, such as light irradiation or voltage application, the equilibrium state is restored by recombination between minority carriers and majority carriers. In this case, the recombination process causes luminescence or thermal energy generation. There are several kinds of carrier recombination processes, such as direct recombination, Auger recombination, Shockley-Read-Hall (SRH) recombination, trap-assisted recombination, surface recombination, and radiative recombination.

Direct recombination [64] is the process by which an electron in the conduction band and a hole in the valence band recombine directly through the band gap. Generally, it appears in direct-transition semiconductors such as gallium arsenide (GaAs) and gallium nitride (GaN) [65].

Auger recombination is a recombination process in which the recombination energy of electrons and holes is supplied to a third carrier. In general, Auger recombination is an important recombination process when the carrier density is very high, such as at high doping concentrations or in high-level injection states [66–68].

SRH recombination is a recombination process through recombination centers, which are localized levels between bands. Typically, this recombination center is located in the middle of the band gap [63,69–72]. In indirect transition semiconductors, such as silicon carbide (SiC) [67,68,71], SRH recombination is the main recombination process compared to direct recombination. Since carrier transition probability depends on the energy difference between transition levels, recombination centers increase the recombination probability.

Trap-assisted recombination is a special case of SRH recombination. When the semiconductor is doped by the donor or acceptor, or the regular periodicity of the crystal is destroyed, the trap energy level will be introduced between the band gap. Generally, at low temperatures, minority carriers will be captured into the trap and then recombined with the majority carriers [65,73].

Surface recombination is also one of the special SRH recombination. On the surface of a semiconductor, the crystal structure becomes discontinuous, and atoms at the edges have no covalent bonding partners. Therefore, at the surface of semiconductor materials, defect states or traps can be generated. Most of the defects or traps will become the surface recombination center to enhance recombination at the surface. Additionally, most of the chemical reactions occur at the surface or the interface between semiconductors and electrolytes [32]. Therefore, surface recombination can dominate the performance of semiconductor devices.

Radiative recombination is a recombination process in which the recombination energy of electrons and holes is emitted as the luminescence. Similar to SRH recombination and surface recombination, it is also recombination through a recombination center which is called the radiative recombination center other than direct recombination. Therefore, it is extensively studied in applications such as light-emitting diodes (LEDs) or lasers.

Carrier lifetime is the average time of carrier recombination. Various factor can affect

the carrier lifetime, such as excited wavelength [63,70,71], excited carrier concentration [63,74], temperature [63,67,68,71], doping density [32,70], and crystal faces [63,70,72]. By analyzing and integrating each factor's dependence on carrier lifetime, we can define the dominant recombination process for each material. In addition, the carrier lifetime can directly affect the STH energy conversion efficiency [32]. Therefore, we can consider the suitable carrier lifetime to improve the performance of semiconductors for their applications.

1.3.2 Characterization methods

1.3.2.1 Microwave photoconductivity decay (μ-PCD)

μ-PCD is the most widely employed technique to measure the carrier lifetime because it is both insensitive to surface roughness and sensitive to signals from excited carriers [75,76]. This method evaluates excess carrier attenuation by observing the conductivity change of a sample from the intensity of microwaves reflected from the sample.

When the carriers are excited, the conductivity of the material changes. Since the reflectance of microwaves is directly proportional to the conductivity of the sample, the carrier recombination process is expressed by detecting changes in microwave reflectance.

1.3.2.3 Photoluminescence (PL) spectra

PL refers to the luminescence emitted when excess carriers excited by the absorption of photons recombine. As mentioned above in 1.3.1, When emitted in the form of luminescence, it is called radiative recombination, and the luminescence emitted by radiative recombination resulting from optical excitation such as laser is PL. The radiative recombination process includes not only direct recombination but also recombination through defect and impurity energy levels, and this information is

reflected in the PL wavelength [65,73]. Therefore, it is possible to identify defect and impurity energy levels in a material by analyzing the PL spectra.

1.3.2.2 Time-resolved photoluminescence (TR-PL)

TR-PL is another common technique to measure carrier lifetime [76]. This method evaluates the attenuation of excess carriers by generating excess carriers by irradiating pulsed light with energy larger than the band gap of the semiconductor and detecting the transient characteristics of the PL emitted during the recombination process [77].

TR-PL measure corresponding to the PL spectra has a high signal and is sensitive to the luminescent material which is the direct transition semiconductor compared to the indirect transition semiconductor, especially in the perovskite solar cells.

1.4 Material properties in this work

1.4.1 Titanium oxide (TiO$_2$)

TiO$_2$ is one of the stable photocatalysts which has three crystal structures: anatase, rutile, and brookite [78–81]. Among these structures, with a band gap of 3.2 eV for anatase and 3.0 eV for rutile, are widely used in different fields in the industry. However, similarly, they can only absorb the ultraviolet region of solar light resulting in low energy conversion efficiency. Generally, TiO$_2$ is an insulator at room temperature. However, when irradiating the solar light, it will become an n-type semiconductor.

The anatase type is stable at low temperatures and starts to transform into the rutile type at about 600°C [82–84]. On the other hand, the rutile type has the most stable structure even at high temperatures, providing good single-crystalline quality. Contributing to the properties of insolubility in other acids, alkalis, water, and organic solvents, it can be used not only in photocatalytic water splitting but also in dye-sensitized solar cells. However, it can be soluble in hydrofluoric acid, hot concentrated sulfuric acid and molten alkali salts, therefore, little applications are limited.

In general, rutile TiO_2 single crystal is grown by the Verneuil method [85,86], the Floating Zone method [87,88], and the Edge-defined Film Growth method [89]. Among these methods, the Verneuil method is the most prevalent and commercially viable due to its high growth speed and low manufacturing cost. Single crystals produced using this method are commonly employed as optical prisms or as a substrate for epitaxial growth.

1.4.2 Cubic silicon carbide (3C-SiC)

SiC stands out as one of the earliest compound semiconductors in history and has been extensively studied to date. It has three polytypes: 3C-SiC, 4H-SiC, and 6H-SiC. Among them, 3C-SiC is cubic structure, while 4H- and 6H-SiC is hexagonal structure. With different structures, the band gap differs, thus, the application region differs. The band gap of 3C-SiC is 2.3 eV, therefore, it can act as a visible-light photocatalyst [34,90–92]. However, for 4H-SiC, with a band gap of 3.2 eV, it is widely applied for power devices [93,94].

In photocatalytic water splitting, 3C-SiC becomes one of the most promising material owing to its durability [92]. Recently, p-type 3C-SiC has drawn wide attention as the photoelectrode under visible light. Moreover, in order to improve the photocatalytic performance of 3C-SiC, platinum (Pt) co-catalyst-loaded photoelectrode shows a higher STH energy conversion efficiency [95,96], however, the photocurrent is still small. Recently, a new texture structure has been developed to improve the photocurrent [90]. Using this structure, the irradiated light is absorbed by the material after several reflections on the surface of the material, thus increasing the utilization of light. Moreover, this structure also increases the contact area with the solution, thus increasing the area of the chemical reaction. If this structure can be improved deeply, the application of 3C-SiC on photocatalysis will be improved by various processing or surface treatments and it's worth being expected to be widely used.

1.4.3 Bismuth vanadate (BiVO₄)

BiVO₄ has garnered significant attention and has been extensively researched as a compelling material for photocatalysts, particularly in applications related to solar-driven water splitting for hydrogen production. The absorption properties of BiVO₄ are suitable for employing visible light: for instance, tetragonal and monoclinic crystals have band gaps of 2.9 eV and 2.4 eV [97–99]. Among them, the monoclinic BiVO₄ is more promising owing to its smaller bandgap [100–102]. Similar to 3C-SiC, with this narrow band gap, it can act as a visible-light photocatalyst.

Nowadays, the BiVO₄ semiconductor has been widely and successfully employed as a water oxidation photocatalyst in the assembly of Z-scheme overall water splitting (OWS) systems due to its advantageous characteristics, including efficient light absorption in the visible light region, good carrier mobility, controllable exposed facets, and non-toxic properties [98]. Therefore, it is worth being expected as well.

1.4.4 Strontium titanate (SrTiO₃)

SrTiO₃ is a cubic perovskite oxide with a band gap of 3.2 eV, and it showcases promising photocatalytic activity, particularly in water-splitting reactions [103–105]. SrTiO3 has similar features to those of TiO₂, such as a wide band gap, corrosion resistance, and heat resistance. Similarly, SrTiO₃ single crystal is also grown using the Verneuil method [106–108], and the Floating Zone method [109,110].

Recently, the K. Domen group has reported a significant breakthrough for SrTiO₃ in 2020. A large-scale 100-m² array of panel reactors consisting of aluminum (Al) -doped SrTiO₃ particulate photocatalyst operate safely for several months and use commercial polyimide membranes to autonomously recover hydrogen from moist [111]. Although the STH of 0.76% is comparable to other systems, their safety and durability are optimized. Their work has a positive effect on photocatalytic applications. It is a great contribution to the development and enhancement of SrTiO₃.

1.4.5 Cerium oxide (CeO$_2$)

CeO$_2$ has been extensively studied as a compelling semiconductor, and various methodologies have been employed to enhance its performance in applications such as CO or CO$_2$ reduction, photo-electrocatalytic processes, and heterogeneous catalysis [112,113]. These applications are possible owing to its fluorite structure and a wide band gap of 3.2 eV (absorption edge: approximately 387 nm) [114,115].

Various methods are utilized to synthesize CeO$_2$. Hydrothermal and sonochemical synthesis methods are commonly employed for the fabrication of CeO$_2$ nanoparticles [116,117]. Presently, a wide range of biological resources, including plants, microbes, and other biological products, are being utilized in the green synthesis of CeO$_2$ nanoparticles [118]. Therefore, if CeO$_2$ can be widely applied using such an echo-friendly method, it will make great strides in photocatalysis.

1.5 Preview of the thesis

The aim of this thesis is to explain the relationship between charge carrier dynamics and photocatalytic performance, then build a tandem structure system to achieve efficient hydrogen production, and finally, find more efficient photocatalysts that can be employed in this system. TiO$_2$, 3C-SiC, BiVO$_4$, SrTiO$_3$, and CeO$_2$ are utilized for characterization in this work.

In summary, this thesis comprises six chapters. In the first chapter, overviews of hydrogen energy, production methods, and charge carrier dynamics are introduced. The simple properties of the materials in this work are also introduced.

In the second chapter, the pH and irradiated light intensity dependence of tandem structure combined with TiO$_2$ and 3C-SiC single crystals are characterized. The gas generation is also completed. Moreover, the long-term durability is also tested.

In the third chapter, the injected photon density and temperature dependence of

carrier life of $BiVO_4$ single crystals on different crystal faces are measured using the μ-PCD method. Then, using the diffusion equations, the surface recombination velocities and bulk lifetime are estimated.

In the fourth chapter, the injected photon density and temperature dependence of carrier recombination for polished and unpolished TiO_2 and $SrTiO_3$ single crystals are measured. Moreover, chemical characterization and dislocation observation are present. Finally, the photoelectrochemical properties are measured.

In the fifth chapter, the PL spectra is observed using a CeO_2 single crystal. Moreover, the temperature dependence of TR-PL results are compared. Finally, using rate equations, the trap energy level of defects and the capture cross-section of majority carriers are estimated.

Finally, in the sixth chapter, the conclusion and the future work outlook are included.

References

[1] M. Rosen, *Int. J. Hydrog. Energy*, **16**, 207–217 (1991).

[2] A. Simpson and A. Lutz, *Int. J. Hydrog. Energy*, **32**, 4811–4820 (2007).

[3] L. Barelli, G. Bidini, F. Gallorini, and S. Servili, *Energy*, **33**, 554–570 (2008).

[4] Y. Yao, *J. Catal.*, **87**, 152–162 (1984).

[5] D. Dissanayake, *J. Catal.*, **132**, 117–127 (1991).

[6] F. Dawood, M. Anda, and G.M. Shafiullah, *Int. J. Hydrog. Energy*, **45**, 3847–3869 (2020).

[7] E. Shoko, B. McLellan, A.L. Dicks, and J.C.D. Da Costa, *Int. J. Coal Geol.*, **65**, 213–222 (2006).

[8] K. Yamashita and L. Barreto, *Energy*, **30**, 2453–2473 (2005).

[9] R. De Levie, *J. Electroanal. Chem.*, **476**, 92–93 (1999).

[10] W. Kreuter, *Int. J. Hydrog. Energy*, **23**, 661–666 (1998).

[11] R. Leroy, *Int. J. Hydrog. Energy*, **8**, 401–417 (1983).

[12] I. Roger, M.A. Shipman, and M.D. Symes, *Nat. Rev. Chem.*, **1**, 0003 (2017).

[13] S. Marini, P. Salvi, P. Nelli, R. Pesenti, M. Villa, M. Berrettoni, G. Zangari, and Y. Kiros, *Electrochimica Acta*, **82**, 384–391 (2012).

[14] J. Brauns and T. Turek, *Processes*, **8**, 248 (2020).

[15] L. Chen, X. Dong, Y. Wang, and Y. Xia, *Nat. Commun.*, **7**, 11741 (2016).

[16] K. Zeng and D. Zhang, *Prog. Energy Combust. Sci.*, **36**, 307–326 (2010).

[17] M. Carmo, D.L. Fritz, J. Mergel, and D. Stolten, *Int. J. Hydrog. Energy*, **38**, 4901–4934 (2013).

[18] P. Millet, N. Mbemba, S.A. Grigoriev, V.N. Fateev, A. Aukauloo, and C. Etiévant, *Int. J. Hydrog. Energy*, **36**, 4134–4142 (2011).

[19] S. Shiva Kumar and V. Himabindu, *Mater. Sci. Energy Technol.*, **2**, 442–454 (2019).

[20] T. Wang, X. Cao, and L. Jiao, *Carbon Neutrality*, **1**, 21 (2022).

[21] A. Brisse, J. Schefold, and M. Zahid, *Int. J. Hydrog. Energy*, **33**, 5375–5382 (2008).

[22] G. Schiller, A. Ansar, M. Lang, and O. Patz, *J. Appl. Electrochem.*, **39**, 293–301 (2009).

[23] A. Hauch, S.D. Ebbesen, S.H. Jensen, and M. Mogensen, *J. Mater. Chem.*, **18**, 2331 (2008).

[24] T. Holm, T. Borsboom-Hanson, O.E. Herrera, and W. Mérida, *Energy Convers. Manag.*, **237**, 114106 (2021).

[25] A. Fujishima and K. Honda, *Nature*, **238**, 37–38 (1972).

[26] Z. Wang, C. Li, and K. Domen, *Chem. Soc. Rev.*, **48**, 2109–2125 (2019).

[27] K. Maeda and K. Domen, *J. Phys. Chem. Lett.*, **1**, 2655–2661 (2010).

[28] S.Y. Tee, K.Y. Win, W.S. Teo, L. Koh, S. Liu, C.P. Teng, and M. Han, *Adv. Sci.*, **4**, 1600337 (2017).

[29] K. Maeda, *J. Photochem. Photobiol. C Photochem. Rev.*, **12**, 237–268 (2011).

[30] I.M. Kolthoff and F.G. Thomas, *J. Phys. Chem.*, **69**, 3049–3058 (1965).

[31] D.Hyun. Kim and M.A. Anderson, *Environ. Sci. Technol.*, **28**, 479–483 (1994).

[32] M. Kato, H. Najima, and T. Ozawa, *J. Electrochem. Soc.*, **166**, H468–H472 (2019).

[33] H. Reiss and A. Heller, *J. Phys. Chem.*, **89**, 4207–4213 (1985).

[34] E. Zhang, Z. Liu, and M. Kato, *Sol. Energy Mater. Sol. Cells*, **230**, 111260 (2021).

[35] Z. Cao, Q. Chen, J. Zhang, H. Li, Y. Jiang, S. Shen, G. Fu, B. Lu, Z. Xie, and L. Zheng, *Nat. Commun.*, **8**, 15131 (2017).

[36] H. Suzuki, A. Hiratsuka, S. Sasaki, and I. Karube, *Sens. Actuators B Chem.*, **46**, 104–113 (1998).

[37] G.A. East and M.A. Del Valle, *J. Chem. Educ.*, **77**, 97 (2000).

[38] B.J. Polk, A. Stelzenmuller, G. Mijares, W. MacCrehan, and M. Gaitan, *Sens. Actuators B Chem.*, **114**, 239–247 (2006).

[39] L.J. Minggu, W.R. Wan Daud, and M.B. Kassim, *Int. J. Hydrog. Energy*, **35**, 5233–5244 (2010).

[40] B. You and Y. Sun, *Acc. Chem. Res.*, **51**, 1571–1580 (2018).

[41] L. Zhang, J. Zhang, H. Yu, and J. Yu, *Adv. Mater.*, **34**, 2107668 (2022).

[42] X. Li, J. Wen, J. Low, Y. Fang, and J. Yu, *Sci. China Mater.*, **57**, 70–100 (2014).

[43] H. Abdullah, Md.M.R. Khan, H.R. Ong, and Z. Yaakob, *J. CO2 Util.*, **22**, 15–32 (2017).

[44] S.-Y. Lee and S.-J. Park, *J. Ind. Eng. Chem.*, **19**, 1761–1769 (2013).

[45] K.M. Lee, C.W. Lai, K.S. Ngai, and J.C. Juan, *Water Res.*, **88**, 428–448 (2016).

[46] F. Motahari, M.R. Mozdianfard, F. Soofivand, and M. Salavati-Niasari, *RSC Adv.*, **4**, 27654 (2014).

[47] D. Friedmann, A. Hakki, H. Kim, W. Choi, and D. Bahnemann, *Green Chem.*, **18**, 5391–5411 (2016).

[48] S. Gisbertz and B. Pieber, *ChemPhotoChem*, **4**, 456–475 (2020).

[49] J. Chen, J. Cen, X. Xu, and X. Li, *Catal. Sci. Technol.*, **6**, 349–362 (2016).

[50] M. Li, Y. Liu, L. Dong, C. Shen, F. Li, M. Huang, C. Ma, B. Yang, X. An, and W. Sand, *Sci. Total Environ.*, **668**, 966–978 (2019).

[51] Y. Liu, J. Li, B. Zhou, X. Li, H. Chen, Q. Chen, Z. Wang, L. Li, J. Wang, and W. Cai, *Water Res.*, **45**, 3991–3998 (2011).

[52] K. Li, Y. Xu, Y. He, C. Yang, Y. Wang, and J. Jia, *Environ. Sci. Technol.*, **47**, 3490–3497 (2013).

[53] S. Fang, M. Rahaman, J. Bharti, E. Reisner, M. Robert, G.A. Ozin, and Y.H. Hu, *Nat. Rev. Methods Primer*, **3**, 61 (2023).

[54] J. Ran, M. Jaroniec, and S. Qiao, *Adv. Mater.*, **30**, 1704649 (2018).

[55] K. Takanabe, *ACS Catal.*, **7**, 8006–8022 (2017).

[56] D. Zhang, G. Li, X. Yang, and J.C. Yu, *Chem. Commun.*, 4381 (2009).

[57] S. Kwon, M. Fan, A.T. Cooper, and H. Yang, *Crit. Rev. Environ. Sci. Technol.*, **38**, 197–226 (2008).

[58] H. Tong, S. Ouyang, Y. Bi, N. Umezawa, M. Oshikiri, and J. Ye, *Adv. Mater.*, **24**, 229–251 (2012).

[59] D. Yang, H. Liu, Z. Zheng, Y. Yuan, J. Zhao, E.R. Waclawik, X. Ke, and H. Zhu, *J. Am. Chem. Soc.*, **131**, 17885–17893 (2009).

[60] J. Low, B. Dai, T. Tong, C. Jiang, and J. Yu, *Adv. Mater.*, **31**, 1802981 (2019).

[61] S. Ikeda, N. Sugiyama, S. Murakami, H. Kominami, Y. Kera, H. Noguchi, K. Uosaki, T. Torimoto, and B. Ohtani, *Phys. Chem. Chem. Phys.*, **5**, 778–783 (2003).

[62] P. Sun, Z. Xing, Z. Li, and W. Zhou, *Chem. Eng. J.*, **458**, 141399 (2023).

[63] E. Zhang and M. Kato, *J. Phys. Appl. Phys.*, **56**, 025103 (2023).

[64] J.P. Bergman, O. Kordina, and E. Janzén, *Phys. Status Solidi A*, **162**, 65–77 (1997).

[65] M. Kato, T. Asada, T. Maeda, K. Ito, K. Tomita, T. Narita, and T. Kachi, *J. Appl. Phys.*, **129**, 115701 (2021).

[66] J. Linnros, *J. Appl. Phys.*, **84**, 284–291 (1998).

[67] K. Tanaka and M. Kato, *AIP Adv.*, **13**, 085220 (2023).

[68] K. Tanaka, K. Nagaya, and M. Kato, *Jpn. J. Appl. Phys.*, **62**, SC1017 (2023).

[69] M. Kato and Y. Kato, *Chem. Phys. Lett.*, **805**, 139955 (2022).

[70] M. Kato, T. Ozawa, and Y. Ichikawa, *J. Phys. Appl. Phys.*, **54**, 345106 (2021).

[71] M. Kato, Z. Xinchi, K. Kohama, S. Fukaya, and M. Ichimura, *J. Appl. Phys.*, **127**, 195702 (2020).

[72] M. Kato, K. Kohama, Y. Ichikawa, and M. Ichimura, *Mater. Lett.*, **160**, 397–399 (2015).

[73] M. Kato, T. Maeda, K. Ito, K. Tomita, T. Narita, and T. Kachi, *Jpn. J. Appl. Phys.*, **61**, 078004 (2022).

[74] M. Kato, A. Ogawa, L. Han, and T. Kato, *Mater. Sci. Semicond. Process.*, **170**, 107980 (2024).

[75] T. Asada, Y. Ichikawa, and M. Kato, *J. Vis. Exp.*, 59007 (2019).

[76] P. Ščajev, S. Miasojedovas, L. Subačius, K. Jarašiūnas, A.V. Mazanik, O.V. Korolik, and M. Kato, *J. Lumin.*, **212**, 92–98 (2019).

[77] Y. Li, Z. Jia, Y. Yang, F. Yao, Y. Liu, and Q. Lin, *Appl. Phys. Rev.*, **10**, 011406 (2023).

[78] D.R. Eddy, M.D. Permana, L.K. Sakti, G.A.N. Sheha, Solihudin, S. Hidayat, T. Takei, N. Kumada, and I. Rahayu, *Nanomaterials*, **13**, 704 (2023).

[79] P. Oruç, N. Turan, S. Cavdar, N. Tuğluoğlu, and H. Koralay, *J. Mater. Sci. Mater. Electron.*, **34**, 498 (2023).

[80] L. Ma, Y. Zhang, S. Zhang, L. Wang, C. Zhang, Y. Chen, Q. Wu, L. Chen, L. Zhou, and W. Wei, *Adv. Funct. Mater.*, 2305788 (2023).

[81] X. Zhu, F. Qin, Y. Luo, L. Zhang, D. Yang, W. Feng, and S. Chen, *J. Mol. Struct.*, **1294**, 136440 (2023).

[82] D.-J. Won, C.-H. Wang, H.-K. Jang, and D.-J. Choi, *Appl. Phys. Mater. Sci. Process.*, **73**, 595–600 (2001).

[83] R. Su, R. Bechstein, L. Sø, R.T. Vang, M. Sillassen, B. Esbjörnsson, A. Palmqvist, and F. Besenbacher, *J. Phys. Chem. C*, **115**, 24287–24292 (2011).

[84] P.I. Gouma and M.J. Mills, *J. Am. Ceram. Soc.*, **84**, 619–622 (2001).

[85] X. Liu, H. Ma, L. Wang, Y. Hu, and X. Sun, *J. Cryst. Growth*, **623**, 127403 (2023).

[86] L. Wang, X. Liu, X. Bi, Z. Ma, J. Li, and X. Sun, *Ceram. Int.*, **48**, 30240–30248 (2022).

[87] J. Rodrigues, M. Peres, A.J.S. Fernandes, M.P.F. Graça, N.A. Sobolev, F.M. Costa, and T. Monteiro, *Appl. Surf. Sci.*, **258**, 9143–9147 (2012).

[88] K.K. Bamzai, S.M. Koohpayeh, B. Kaur, D. Fort, and J.S. Abell, *Ferroelectrics*, **377**, 1–21 (2008).

[89] H. Machida, K. Hoshikawa, and T. Fukuda, *J. Cryst. Growth*, **128**, 829–833 (1993).

[90] M. Kato and T. Ambe, *Appl. Phys. Express*, **13**, 026506 (2020).

[91] M. Kato, *ECS Trans.*, **80**, 43–55 (2017).

[92] N. Ichikawa, M. Ichimura, and M. Kato, *Int. J. Hydrog. Energy*, **42**, 22698–22703 (2017).

[93] T. Fukui, T. Ishii, T. Tawara, K. Takenaka, and M. Kato, *Jpn. J. Appl. Phys.*, **62**, 016508 (2023).

[94] M. Kato, O. Watanabe, T. Mii, H. Sakane, and S. Harada, *Sci. Rep.*, **12**, 18790 (2022).

[95] N. Ichikawa, M. Kato, and M. Ichimura, *Appl. Phys. Lett.*, **109**, 153904 (2016).

[96] A. Paracchino, V. Laporte, K. Sivula, M. Grätzel, and E. Thimsen, *Nat. Mater.*, **10**, 456–461 (2011).

[97] D.K. Lee and K.-S. Choi, *Nat. Energy*, **3**, 53–60 (2017).

[98] Y. Qi, J. Zhang, Y. Kong, Y. Zhao, S. Chen, D. Li, W. Liu, Y. Chen, T. Xie, J. Cui, C. Li, K. Domen, and F. Zhang, *Nat. Commun.*, **13**, 484 (2022).

[99] Y. Lu, Y. Yang, X. Fan, Y. Li, D. Zhou, B. Cai, L. Wang, K. Fan, and K. Zhang, *Adv. Mater.*, **34**, 2108178 (2022).

[100] T. Takata, J. Jiang, Y. Sakata, M. Nakabayashi, N. Shibata, V. Nandal, K. Seki, T. Hisatomi, and K. Domen, *Nature*, **581**, 411–414 (2020).

[101] X. Zhang, Z. Ai, F. Jia, L. Zhang, X. Fan, and Z. Zou, *Mater. Chem. Phys.*, **103**, 162–167 (2007).

[102] I. Abdellaoui, M.M. Islam, M. Remeika, Y. Higuchi, T. Kawaguchi, T. Harada, C. Budich, T. Maeda, T. Wada, S. Ikeda, and T. Sakurai, *J. Phys. Chem. C*, **124**, 3962–3972 (2020).

[103] K. Iwashina and A. Kudo, *J. Am. Chem. Soc.*, **133**, 13272–13275 (2011).

[104] N. Erdman, K.R. Poeppelmeier, M. Asta, O. Warschkow, D.E. Ellis, and L.D. Marks, *Nature*, **419**, 55–58 (2002).

[105] B. Moss, Q. Wang, K.T. Butler, R. Grau-Crespo, S. Selim, A. Regoutz, T. Hisatomi, R. Godin, D.J. Payne, A. Kafizas, K. Domen, L. Steier, and J.R. Durrant, *Nat. Mater.*, **20**, 511–517 (2021).

[106] Y. Tateno, K. Endo, S. Arisawa, A.-M. Vlaicu, L. Nedelcu, N. Preda, M. Secu, R. Iordanescu, A.C. Kuncser, and P. Badica, *Cryst. Growth Des.*, **19**, 604–612 (2019).

[107] S. Mochizuki, F. Fujishiro, K. Ishiwata, and K. Shibata, *Phys. B Condens. Matter*, **376–377**, 816–819 (2006).

[108] C. Rodenbücher, M. Luysberg, A. Schwedt, V. Havel, F. Gunkel, J. Mayer, and R. Waser, *Sci. Rep.*, **6**, 32250 (2016).

[109] P.I. Nabokin, D. Souptel, and A.M. Balbashov, *J. Cryst. Growth*, **250**, 397–404 (2003).

[110] K. Uematsu, O. Sakurai, N. Mizutani, and M. Kato, *J. Mater. Sci.*, **19**, 3671–3679 (1984).

[111] H. Nishiyama, T. Yamada, M. Nakabayashi, Y. Maehara, M. Yamaguchi, Y. Kuromiya, Y. Nagatsuma, H. Tokudome, S. Akiyama, T. Watanabe, R. Narushima, S. Okunaka, N. Shibata, T. Takata, T. Hisatomi, and K. Domen, *Nature*, **598**, 304–307 (2021).

[112] H.Y. Kim, H.M. Lee, and G. Henkelman, *J. Am. Chem. Soc.*, **134**, 1560–1570 (2012).

[113] E. Kusmierek, *Catalysts*, **10**, 1435 (2020).

[114] C. Yang, Y. Lu, L. Zhang, Z. Kong, T. Yang, L. Tao, Y. Zou, and S. Wang, *Small Struct.*, **2**, 2100058 (2021).

[115] G. Forghieri, D. Zanardo, E. Ghedini, F. Menegazzo, A. Giordana, G. Cerrato,

A. Di Michele, G. Cruciani, and M. Signoretto, *Catalysts*, **11**, 1209 (2021).

[116] A.I.Y. Tok, F.Y.C. Boey, Z. Dong, and X.L. Sun, *J. Mater. Process. Technol.*, **190**, 217–222 (2007).

[117] M. Mousavi-Kamazani and F. Azizi, *Ultrason. Sonochem.*, **58**, 104695 (2019).

[118] M. Nadeem, R. Khan, K. Afridi, A. Nadhman, S. Ullah, S. Faisal, Z.U. Mabood, C. Hano, and B.H. Abbasi, *Int. J. Nanomedicine*, **Volume 15**, 5951–5961 (2020).

Chapter 2

Durable and efficient photoelectrochemical water splitting using TiO_2 and 3C-SiC single crystals in a tandem structure

2.1 Introduction

In recent years, many semiconductor materials have been suggested for use as photocatalysts, however, in photoelectrochemical water splitting, not only the solar-to-hydrogen conversion (STH) efficiency but also the stability and durability of the photoelectrodes are important.

TiO_2 is one of the most durable photocatalyst materials [1–7]. However, as is widely known, its bandgap energy is higher than 3.0 eV, and thus, TiO_2 only absorbs in the near-ultraviolet region of solar light. Silicon carbide (SiC) is another promising photocatalyst material. In particular, p-type cubic SiC (3C-SiC), which has a bandgap energy of 2.3 eV, acts as a durable and efficient photocatalyst for water reduction in the form of photoelectrodes [8–17]. Considering the areal efficiency, it has been found that placing materials with significantly different band gaps in a tandem configuration results in improved efficiency.

In this chapter, we consider employing these materials in a tandem structure, so we can realize the possibility of a self-driven and durable water-splitting system. Although there have been several reports on hybrid photocatalysts consisting of TiO_2 and SiC with nanocrystal or thin-film structures [18–20], there have been no reports on tandem structures using single-crystal photoelectrodes to date. Therefore, we investigate the photochemical properties of TiO_2 photoanode, 3C-SiC photocathode and tandem structure. The applied bias photon-to-current conversion efficiency (ABPE) [16] is also calculated. Furthermore, we observe the amount of hydrogen and oxygen produced and the long-term stability and durability.

2.2 Experimental details

A commercially available n-type single crystal TiO$_2$ (rutile, 0.01 wt% niobium doped) with a (110) surface was used as the photoanode by forming Al ohmic contacts. 3C-SiC was cut from a 30-μm-thick p-type 3C-SiC epitaxial wafer with an Al-doped concentration of 10^{15} cm^{-3}; the wafer was grown on a p$^+$-type 4H-SiC substrate with an inclination of 0.7° toward the $\langle 11\bar{2}0 \rangle$ direction from the (0001) Si face. Ni/Al/Ti ohmic contacts were formed on the substrate side [12]. Pt was electrochemically coated as a cocatalyst onto the 3C-SiC surface at 40 °C with –0.8 mA/cm^2 in a 0.05 M H$_2$PtCl$_6$ and 1 M HCl mixed aqueous solution [16].

Then, we measured the pH dependence and irradiation light intensity dependence of each sample using a three-electrode photoelectrochemical (PEC) system. A TiO$_2$ or 3C-SiC sample was used as the working electrode, a Pt plate was used as the counter electrode, and Ag/AgCl was used as the reference electrode. The potential of the reference electrode was converted to the standard hydrogen electrode (SHE) potential by considering the potential shift due to pH. Hydrochloric acid (HCl) was used to control the acidity, and sodium sulfate (Na$_2$SO$_4$) was used as a solution with neutral pH. The lighting conditions were the result of a solar simulator with 0.05–1 W/cm^2.

We combined the two samples of TiO$_2$ and 3C-SiC into a tandem structure, as shown in Fig. 1. TiO$_2$ was placed onto the light source side and acted as the photoanode; the transmitted light was absorbed by the 3C-SiC photocathode. The photocurrents of the tandem structure were measured without reference electrodes.
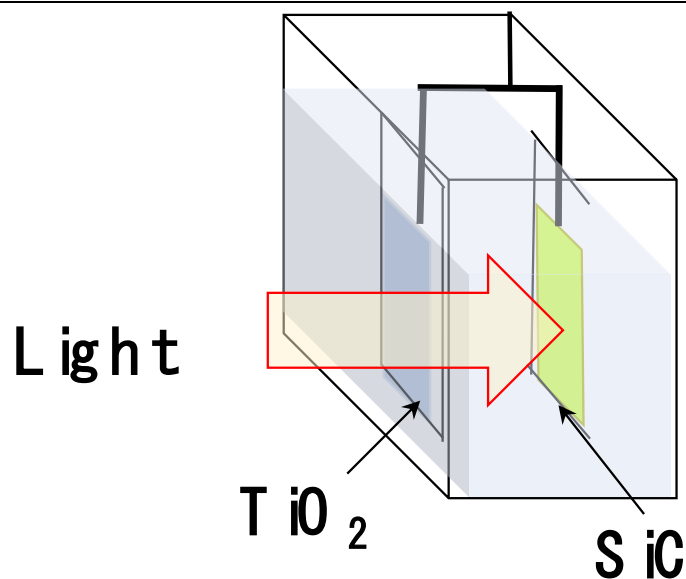
Fig. 1. Schematic of the tandem structure of TiO₂ and 3C-SiC.

We performed a hydrogen generation experiment using a tandem structure. The samples were placed in a sealed container filled with 1 M HCl as electrolyte. An external voltage of 0.4 V was applied during the experiment. For convenience of observation, we increased the irradiated light power to 1 W/cm^2. The oxygen detector (FireSting oxygen monitor) recorded the oxygen volume; the hydrogen volume was analyzed by chromatography (GC-3200 GL Science).

For the long-term durability test, a light-emitting diode (LED) stable light source of 405 nm with a light intensity of 0.5 W/cm^2 was used as excitation light. A Na_2SO_4 solution with a pH of 7 was used as electrolyte for safety. We set the tandem structure into a cell with the Na_2SO_4 solution and connected the samples to a current detector. We also set a solar cell parallel to the tandem cell to monitor the light power stability. The test lasted for approximately 100 days.

2.3 Results and discussion

Figure 2 shows the pH dependence of the photocurrent from the TiO₂ photoanode for an irradiation light intensity of 0.1 W/cm^2. At a lower pH, a photocurrent was observed

at a more negative potential, indicating that the TiO₂ photoanode works effectively at low pH. It has been reported that, at low pH, the surface of TiO₂ shows the following reaction:

$$Ti - O^{2-} + H^+ \rightleftarrows Ti - OH^-$$
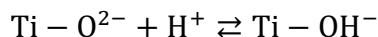
where $Ti - O^{2-}$ denotes a lattice element of the TiO₂ surface, H^+ is a proton in the bulk of the electrolyte solution, and $Ti - OH^-$ is a protonated lattice element [21]. This reaction reduces the number of negative charges on the TiO₂ surface. This reduction in negative charge may enhance the electric field due to the space charge region in TiO₂ which is formed by positively ionized donors. The electric field is a driving force of the photocurrent. Therefore, we consider that, at low pH, photocurrents appear at a more negative potential compared with that at high pH.
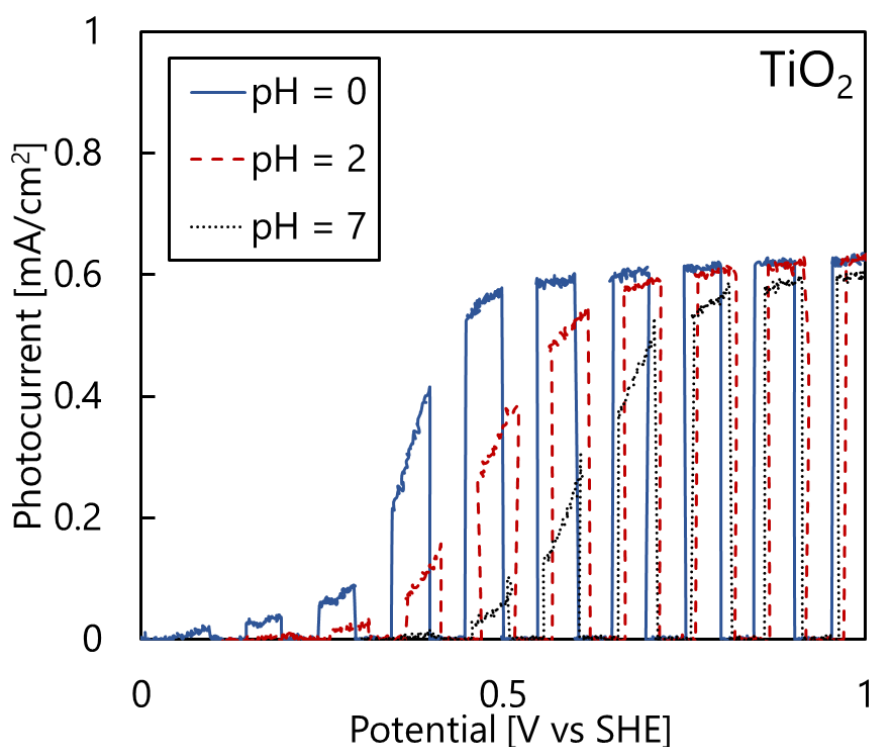
Fig. 2. pH dependence of TiO₂ at an irradiation light intensity of 0.1 W/cm².

Figure 3 shows the pH dependence of the photocurrent from the 3C-SiC photocathode for an irradiation light intensity of 0.1 W/cm². Unlike TiO₂, 3C-SiC

shows a weak pH dependence, and the photocurrent is highest at pH = 0. We observed that, in acidic solutions, the (0001) Si face of 4H-SiC was passivated and surface recombination was suppressed [22]. Therefore, even for our 3C-SiC surface, which has an atomic structure equivalent to that of the 4H-SiC (0001) Si-face, the recombination of carriers is suppressed, resulting in a large photocurrent at pH = 0.
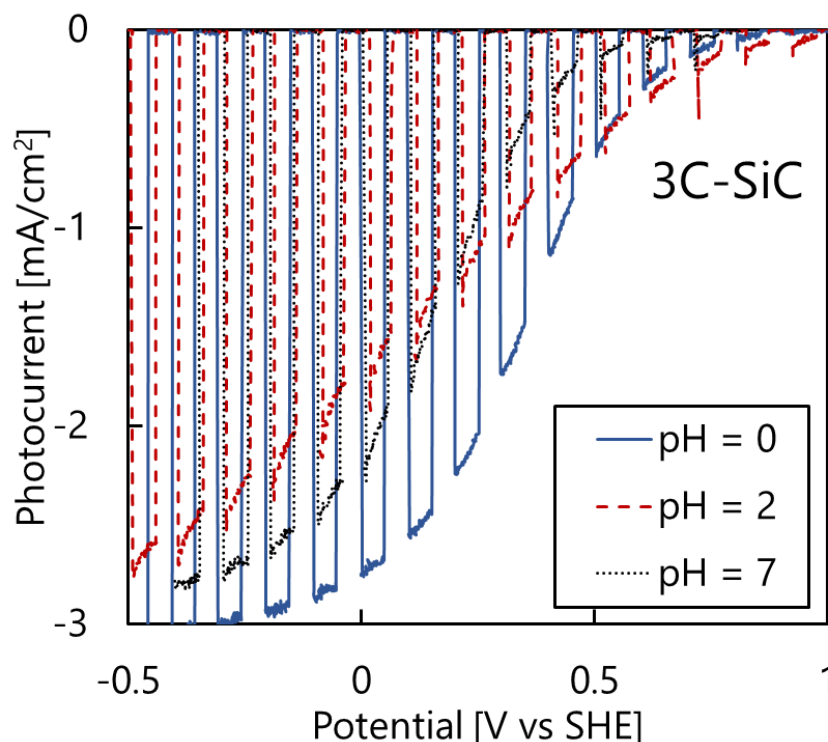
Fig. 3. pH dependence of 3C-SiC at an irradiation light intensity of 0.1 W/cm^2.

Figure 4 shows the pH dependence of the photocurrent from the tandem structure at an irradiation light intensity of 0.1 W/cm^2. The shapes of the current–voltage characteristics of the tandem structure are similar to the current-potential characteristics of TiO$_2$ shown in Fig. 2; at a lower pH, the photocurrent of the tandem structure was larger. The pH affects the surface chemistry of the TiO$_2$ photoanode and the surface recombination of the 3C-SiC photocathode. Both TiO$_2$ and 3C-SiC show large photocurrents at low pH, and thus, the tandem structure also shows a large photocurrent at low pH. In other words, the performance of the tandem structure is high at low pH. In addition, the overall photocurrent of the tandem structure is limited by the smaller

photocurrents from either of the photoelectrodes. As seen in Figs. 2 and 3, photocurrents from the TiO$_2$ photoanode were smaller than those from the 3C-SiC photocathodes; therefore, the photocurrent of the tandem structure is determined by TiO$_2$. Hereafter, we show experimental results at pH = 0 unless otherwise noted.
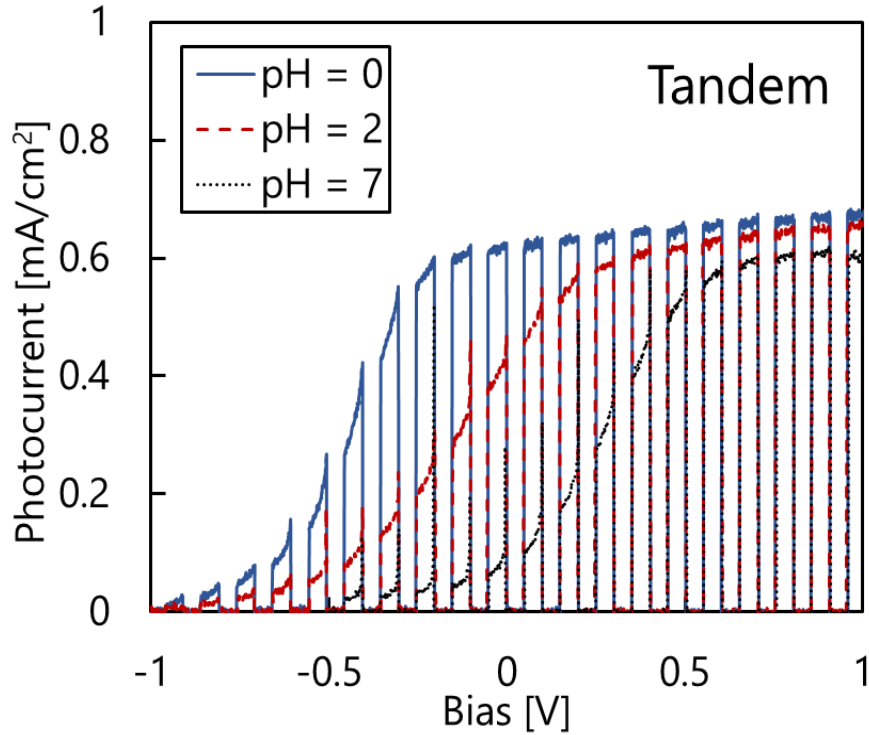
Fig. 4. pH dependence of photocurrent from the tandem structure at an irradiation light intensity of 0.1 W/cm^2.

Using the largest photocurrent observed at a pH of 0, we calculated the ABPE [16] of the tandem structure. The ABPE is calculated using the following formula:

$$\eta \, (\%) \; = \; \frac{(1.23 - |V|) \times |I|}{L}$$

where I is the photocurrent, L is the irradiation light intensity, and 1.23 represents the redox potential width between H$^+$/H$_2$ and O$_2$/H$_2$O. The tandem structure showed a maximum ABPE of 0.74% when no bias was applied.

Figure 5 shows the light intensity dependence of the photocurrent from the TiO$_2$

photoanode and from the 3C-SiC photocathode. TiO$_2$ exhibited a linear dependence, and thus, most of the absorbed photons in TiO$_2$ were converted to photocurrent. However, 3C-SiC showed a sublinear dependence, and we considered two origins for this dependence. First, enhanced electron-hole recombination for a high-level carrier injection resulting in a smaller photocurrent compared with injected photons. The other is limited active sites at the 3C-SiC surface for the photocurrent, as Pt was loaded onto the 3C-SiC surface as active sites for the hydrogen reduction. Although electron-hole pairs increased with high-intensity light, the number of Pt is limited. Therefore, the increase in photocurrent gradually saturated at high light intensity. The inset of Fig. 5 shows the light intensity dependence of the photocurrent in the tandem structure. The tandem structure showed linear light intensity dependence for the photocurrent. Thus, the photocurrent from the tandem structure is dominated by the photocurrent from the TiO$_2$ photoanode, as observed in the pH dependence.
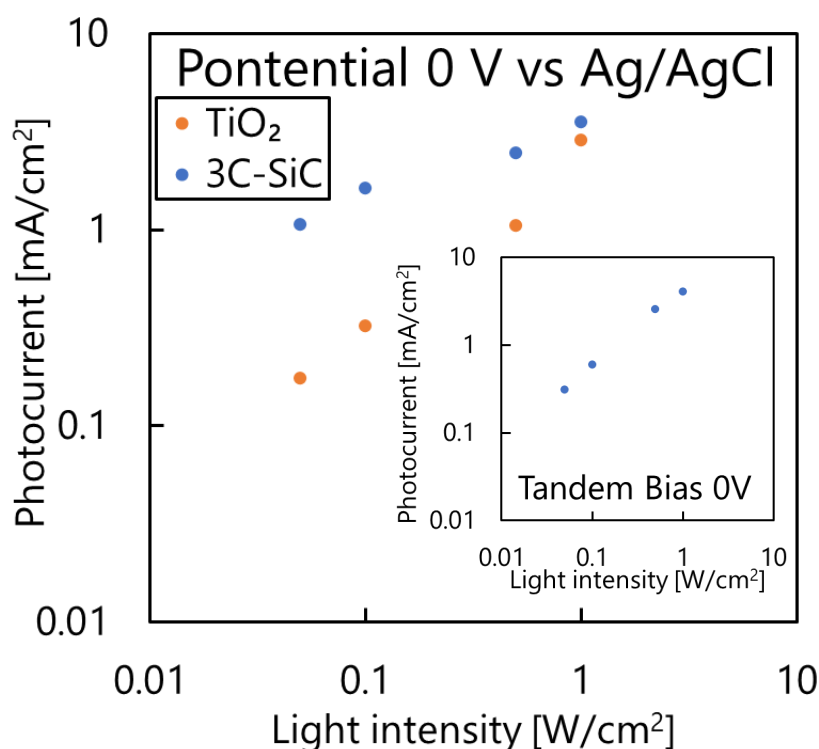
Fig. 5. Light intensity dependence of photocurrents from TiO$_2$ and 3C-SiC. The inset shows the irradiation light intensity dependence of the photocurrent from the tandem structure.

Figure 6 shows the photocurrent from the tandem structure up to 1800 s; the inset shows the corresponding generated gases. To enhance gas generation for an accurate detection of the volumes, we adopted an irradiation of 1 W/cm² and applied a bias of 0.4 V to the tandem structure. The photocurrent of ~4.75 mA/cm² remained stable during the experiment. The predicted hydrogen and oxygen production were consistent with the detected volumes. Therefore, most photocurrents from the tandem structure contributed to water splitting with the generation of oxygen and hydrogen.
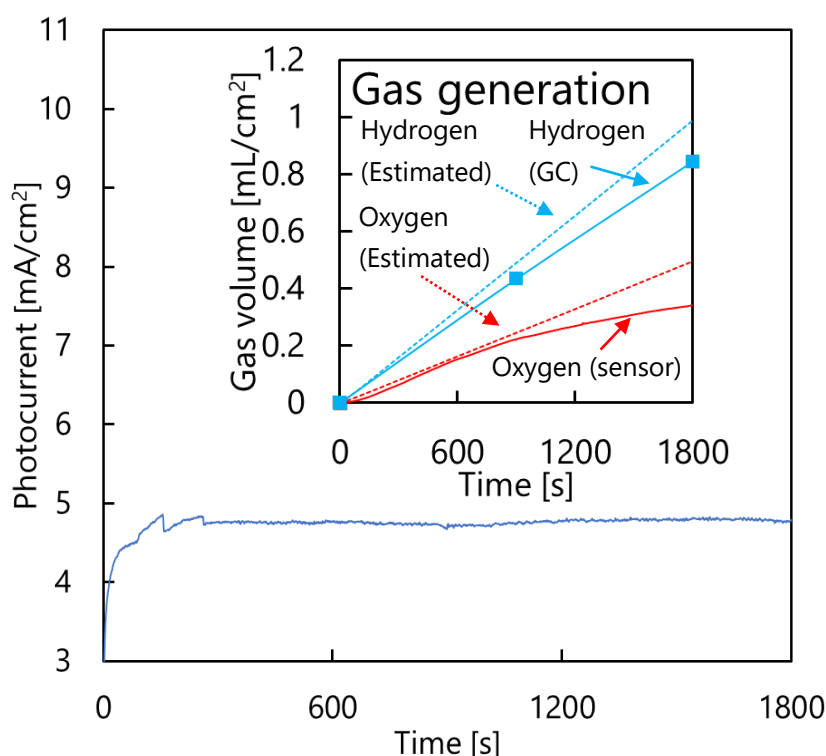
Fig. 6. Photocurrent from the tandem structure irradiated by a light intensity of 1 W/cm² with an applied bias of 0.4 V up to 1800 s. The inset shows volumes of hydrogen and oxygen gases.

Figure 7 shows the durability of the photocurrent from the tandem structure with an LED light source of 405 nm and 0.5 W/cm². The photocurrent from the tandem structure was stable during the experiment; the light intensity was also stable, as monitored by the solar cell. Therefore, the TiO₂ and 3C-SiC tandem structures were durable for at least 100 days.
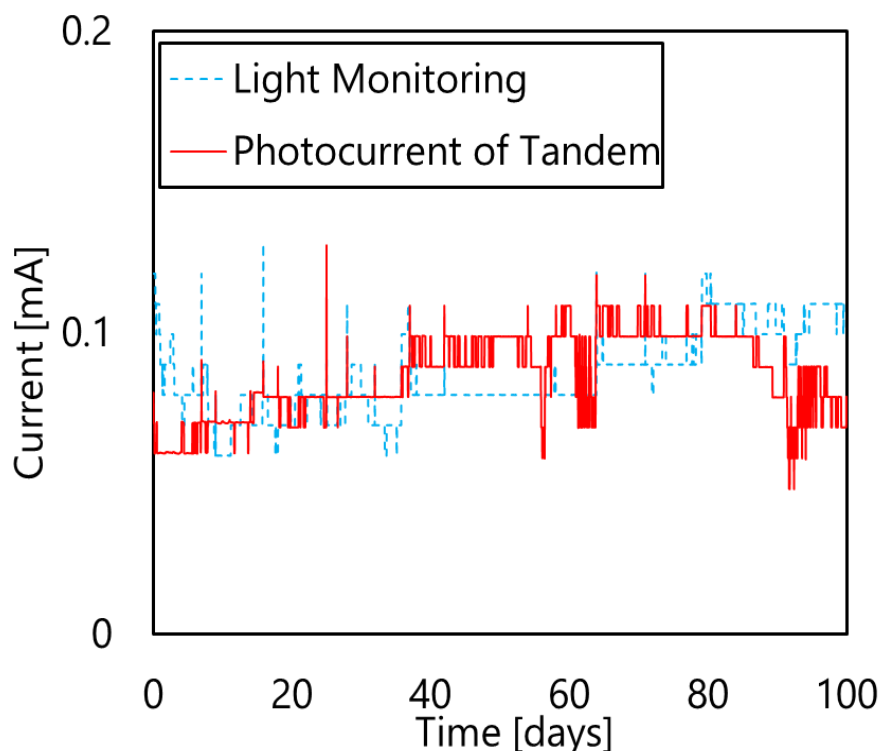
Fig. 7. Photocurrent from the tandem structure illuminated by LED in 1 M Na₂SO₄
solution without bias.

Table 1 summarizes the reported values for STH/ABPE and durability of our results. Our 0.74% of ABPE is comparable to the reported STH/ABPE. Regarding durability, most of the confirmed periods are within 10 h to 21 days [23–36], and the longest period was for GaN:ZnO solid solution photocatalysts, which remain stable for ~90 days [37]. Our tandem structure shows durability for almost the same period as that of the GaN:ZnO solid solution. The GaN:ZnO solid solution photocatalysts showed good durability because the bond energies of Ga-N (876.9 kJ/mol) and Zn-O (250 kJ/mol) are strong. Ti-O (667 kJ/mol) and Si-C (435 kJ/mol) also have higher bond energies compared to those of ordinary semiconductors, such as Cd-S (196 kJ/mol), Ga-P (230 kJ/mol), and In-P (197.9 kJ/mol). We consider that such a strong bond contributes to the long-term durability of TiO₂ and 3C-SiC, which is similar to that of GaN:ZnO. Therefore, a tandem structure with a TiO₂ photoanode and a 3C-SiC photocathode exhibits a durability and efficiency comparable to other state-of-the-art photocatalytic water splitting systems.

Table 1. Summary of reported STH/ABPE and durability

Materials	STH/ABPE (%)	Durability (h)
Ag/WO$_3$ [24]	0.09	10
Pt-modified BaTaO$_2$N [25]	0.24	10.2
TiO$_2$/CoOOH/RhCrOx/SrTiO$_3$:Al [26]	0.3	1300 (approximately 54.2 days)
Sb$_2$Se$_3$/ BiVO$_4$ [27]	1.5	10
Vs-CIS-500 [28]	2.49	15
NiFeO$_x$/B-C$_3$N$_4$/Mo-BiVO$_4$ [29]	2.67	10
InGaP/GaAs double junction [30]	9	150
NiCo$_2$S$_4$-4//NiCo$_2$S$_4$-4 [23]	18.01	72
FeCoNi-HNTAs [31]		100 (approximately 4.17 days)
Ni(OH)$_2$–PtO$_2$ NS/Ti [32]		100 (approximately 4.17 days)
CoNC/GD [34]		120 (5 days)
carbon fiber paper integrated with		160 (approximately

bifunctional Ni-P [35]		6.67 days)
Pt/CdS/CuGa₃Se₅/ACGSe with CuGa₃Se₅ deposited [33]		480 (20 days)
catalytic β-Mo₂C phase and an acidproof γ-Mo₂N phase [36]		500 (approximately 20.83 days)
GaN: ZnO solid solution photocatalyst modified with Rh₂₋ᵧCrᵧO₃ nanoparticles [37]		2160 (approximately 90 days)
this work	0.74	2400 (100 days)

2.4 Conclusions

We measured the pH dependence and irradiation light intensity dependence of photocurrents from TiO₂, 3C-SiC, and the tandem structure. The dependence shows that the performance of the tandem structure is limited by the photocurrent from the TiO₂ photoanode. The maximum ABPE from the tandem structure was 0.74% with no additional bias applied. The efficiency of the system can be improved by improving the TiO₂ photoanode. Gas detection confirmed the generation of hydrogen and oxygen; thus, it was confirmed that the tandem structure can be used for solar water splitting. We also confirmed the durability of the tandem structure for up to 100 d. Therefore, a tandem structure of a TiO₂ photoanode and a 3C-SiC photocathode is a promising system for solar water splitting as it has a high durability and efficiency.

References

[1] A. Fujishima and K. Honda, *Nature*, **238**, 37–38 (1972).

[2] S.U.M. Khan, M. Al-Shahry, and W.B. Ingler, *Science*, **297**, 2243–2245 (2002).

[3] M. Kato, K. Kohama, Y. Ichikawa, and M. Ichimura, *Materials Letters*, **160**, 397–399 (2015).

[4] M. Kato, H. Najima, and T. Ozawa, *J. Electrochem. Soc.*, **166**, H468–H472 (2019).

[5] B. Yang, M. Wang, X. Hu, T. Zhou, and Z. Zang, *Nano Energy*, **57**, 718–727 (2019).

[6] H. Wang, H. Li, W. Cai, P. Zhang, S. Cao, Z. Chen, and Z. Zang, *Nanoscale*, **12**, 14369–14404 (2020).

[7] Z. Chai, J. Gu, Y. Yuan, Z. Zang, and W. Mai, *CrystEngComm*, **17**, 8327–8331 (2015).

[8] T. Yasuda, M. Kato, M. Ichimura, and T. Hatayama, *Appl. Phys. Lett.*, **101**, 053902 (2012).

[9] J. Jian, Y. Shi, S. Ekeroth, J. Keraudy, M. Syväjärvi, R. Yakimova, U. Helmersson, and J. Sun, *J. Mater. Chem. A*, **7**, 4721–4728 (2019).

[10] M. Kato, T. Yasuda, K. Miyake, M. Ichimura, and T. Hatayama, *International Journal of Hydrogen Energy*, **39**, 4845–4849 (2014).

[11] M. Kato, K. Miyake, T. Yasuda, M. Ichimura, T. Hatayama, and T. Ohshima, *Jpn. J. Appl. Phys.*, **55**, 01AC02 (2016).

[12] N. Ichikawa, M. Kato, and M. Ichimura, *Appl. Phys. Express*, **8**, 091301 (2015).

[13] N. Ichikawa, M. Kato, and M. Ichimura, *Applied Physics Letters*, **109**, 153904 (2016).

[14] N. Ichikawa, M. Ichimura, and M. Kato, *International Journal of Hydrogen Energy*, **42**, 22698–22703 (2017).

[15] M. Kato, N. Ichikawa, and Y. Nakano, *Materials Letters*, **254**, 96–98 (2019).

[16] M. Kato and T. Ambe, *Appl. Phys. Express*, **13**, 026506 (2020).

[17] A. Iwase, A. Kudo, Y. Numata, M. Ikegami, T. Miyasaka, N. Ichikawa, M. Kato, H. Hashimoto, H. Inoue, O. Ishitani, and H. Tamiaki, *ChemSusChem*, **10**, 4420–4423 (2017).

[18] J. Zhang, L.Z. Liu, L. Yang, Z.X. Gan, X.L. Wu, and P.K. Chu, *Applied Physics Letters*, **104**, 231902 (2014).

[19] Y. Li, Z. Yu, J. Meng, and Y. Li, *International Journal of Hydrogen Energy*, **38**, 3898–3904 (2013).

[20] R.S. Pessoa, M.A. Fraga, L.V. Santos, M. Massi, and H.S. Maciel, *Materials Science in Semiconductor Processing*, **29**, 56–68 (2015).

[21] T. Watanabe, A. Fujishima, O. Tatsuoki, and K. Honda, *BCSJ*, **49**, 8–11 (1976).

[22] Y. Ichikawa, M. Ichimura, T. Kimoto, and M. Kato, *ECS J. Solid State Sci. Technol.*, **7**, Q127–Q130 (2018).

[23] Z. Kang, H. Guo, J. Wu, X. Sun, Z. Zhang, Q. Liao, S. Zhang, H. Si, P. Wu, L. Wang, and Y. Zhang, *Adv Funct Materials*, **29**, 1807031 (2019).

[24] Y. Li, W. Zhang, and B. Qiu, *Chem. Lett.*, **49**, 741–744 (2020).

[25] Z. Wang, Y. Luo, T. Hisatomi, J.J.M. Vequizo, S. Suzuki, S. Chen, M. Nakabayashi, L. Lin, Z. Pan, N. Kariya, A. Yamakata, N. Shibata, T. Takata, K. Teshima, and K. Domen, *Nat Commun*, **12**, 1005 (2021).

[26] H. Lyu, T. Hisatomi, Y. Goto, M. Yoshida, T. Higashi, M. Katayama, T. Takata, T. Minegishi, H. Nishiyama, T. Yamada, Y. Sakata, K. Asakura, and K. Domen, *Chem. Sci.*, **10**, 3196–3201 (2019).

[27] W. Yang, J.H. Kim, O.S. Hutter, L.J. Phillips, J. Tan, J. Park, H. Lee, J.D. Major, J.S. Lee, and J. Moon, *Nat Commun*, **11**, 861 (2020).

[28] H. Wang, Y. Xia, H. Li, X. Wang, Y. Yu, X. Jiao, and D. Chen, *Nat Commun*, **11**, 3078 (2020).

[29] K.-H. Ye, H. Li, D. Huang, S. Xiao, W. Qiu, M. Li, Y. Hu, W. Mai, H. Ji, and S. Yang, *Nat Commun*, **10**, 3687 (2019).

[30] P. Varadhan, H.-C. Fu, Y.-C. Kao, R.-H. Horng, and J.-H. He, *Nat Commun*, **10**, 5282 (2019).

[31] H. Li, S. Chen, Y. Zhang, Q. Zhang, X. Jia, Q. Zhang, L. Gu, X. Sun, L. Song, and X. Wang, *Nat Commun*, **9**, 2452 (2018).

[32] L. Xie, X. Ren, Q. Liu, G. Cui, R. Ge, A.M. Asiri, X. Sun, Q. Zhang, and L. Chen, *J. Mater. Chem. A*, **6**, 1967–1970 (2018).

[33] L. Zhang, T. Minegishi, M. Nakabayashi, Y. Suzuki, K. Seki, N. Shibata, J. Kubota, and K. Domen, *Chem. Sci.*, **6**, 894–901 (2015).

[34] Y. Xue, J. Li, Z. Xue, Y. Li, H. Liu, D. Li, W. Yang, and Y. Li, *ACS Appl. Mater. Interfaces*, **8**, 31083–31091 (2016).

[35] X. Wang, W. Li, D. Xiong, D.Y. Petrovykh, and L. Liu, *Adv Funct Materials*, **26**, 4067–4077 (2016).

[36] W.-F. Chen, S. Iyer, S. Iyer, K. Sasaki, C.-H. Wang, Y. Zhu, J.T. Muckerman, and E. Fujita, *Energy Environ. Sci.*, **6**, 1818 (2013).

[37] T. Ohno, L. Bai, T. Hisatomi, K. Maeda, and K. Domen, *J. Am. Chem. Soc.*, **134**, 8254–8259 (2012).

Chapter 3

Surface recombination velocities for the (100) and (001) crystal faces of bismuth vanadate single crystals

3.1 Introduction

Bismuth vanadate ($BiVO_4$) has been widely investigated as an attractive material for photocatalysts, and various methods are used to improve the performance of water splitting [1–4]. Because of the visible light absorption, various characterizations have been studied for the properties of $BiVO_4$ [5,6]. Nevertheless, the influence of defects on the properties of this material, including those at the surface, has not been fully comprehended.

The photogenerated carrier lifetime is a crucial material property of photocatalysts, which strongly affects the energy conversion efficiency [7]. As mentioned in Ch. 1, carrier lifetime can be influenced by the surface and defects. Having insight into the lifetime tendencies at surfaces enables the design of material structures for improving energy conversion, achieved by exposing crystal faces with low surface recombination rates [8]. Therefore, we investigate the effect of crystal surfaces on carrier lifetime. Moreover, the characterization of carrier lifetime in high-purity single crystals can show the separate physical properties of both surface and bulk [9].

In this chapter, we consider that different crystal faces will affect the carrier lifetime differently; then, we can realize the different physical properties, respectively. We adopt TR-PL and μ-PCD methods to characterize carrier lifetime in $BiVO_4$. Using different wavelengths of lasers corresponding to different penetration depths, the carrier distribution will be separated. Then, we estimate the surface recombination velocities, S, bulk lifetimes, τ_{bulk}, and recombination center concentration N_r by fitting the obtained μ-PCD decay curves.

35

3.2 Experimental details

Commercial $BiVO_4$ single crystals with a size of $5 \times 5 \times 0.5$ mm with (001) and (100) faces were used as samples which have a chemical purity of around 99.995% and are made by SurfaceNet GmbH.

For the measurements, we used yttrium aluminum garnet (YAG) lasers with wavelengths of 266 and 355 nm and a pulse width of 1 ns as the excitation light sources (FTSS 266-200 and FTSS 355-50, CryLaS). The spot size of the lasers is 0.13 cm^{-2} which is smaller than the samples' size. The intensity is 0.01–0.6 mW for 266 nm laser, and 0.05–4.0 mW for 355 nm laser. The injected photon density was set to 7×10^{12}–5×10^{14} cm^{-2} calculated by laser intensity. The penetration depths in $BiVO_4$ were ~190 nm for the wavelength of 266 nm and ~370 nm for the wavelength of 355 nm [10]. For TR-PL measurements, a photomultiplier was used as a detector [8]. We put a long-pass filter with a cut-off wavelength of 355 nm in front of the photomultiplier. Therefore, the integrated intensity of the TR-PL signal is longer than 355 nm. For μ-PCD measurements, micro-waves at 10 GHz generated from the Gunn diode which has an output power of 50 mW were irradiated to the sample through a waveguide to the unexcited side of the samples as the measurement probe [8,11]. Furthermore, the reflected microwaves from the sample were detected by a Schottky barrier diode. The intensity of the reflected microwaves was converted to a voltage as the signal of the μ-PCD measurement. The details of our μ-PCD measurement system can be seen in [11].

3.3 Results and discussion

Figure 1 shows the injected photon density dependence of the TR-PL decay curves for the (001) face excited by wavelengths of 266 and 355 nm. As shown in this figure, the signal-to-noise ratios of the signals for both the excitation wavelengths were not good.
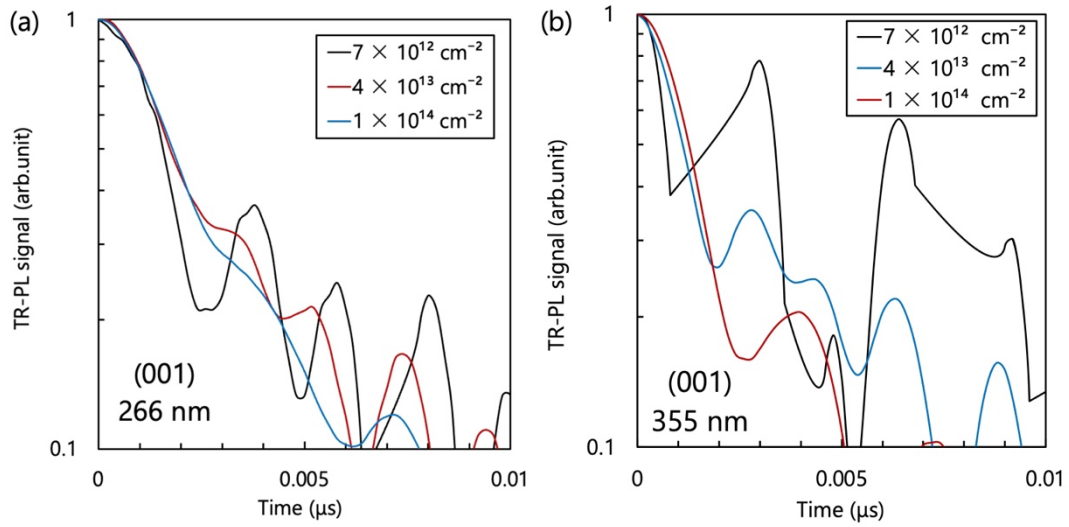
Fig. 1. Injected photon density dependence of TR-PL decay curves on the (001) face at room temperature excited by (a) 266 nm laser and (b) 355 nm laser.

Figure 2 shows the μ-PCD curves on the (001) face excited by wavelengths of 266 and 355 nm at an injected photon density of 7×10^{12} cm^{-2}. The decay for the 266 nm excitation was faster than that at 355 nm. Compared to the TR-PL method, for samples with low excess carrier concentration, the μ-PCD method shows a better signal-to-noise ratio as reported in [12]. Therefore, we adopted μ-PCD results for further analysis and discussion.
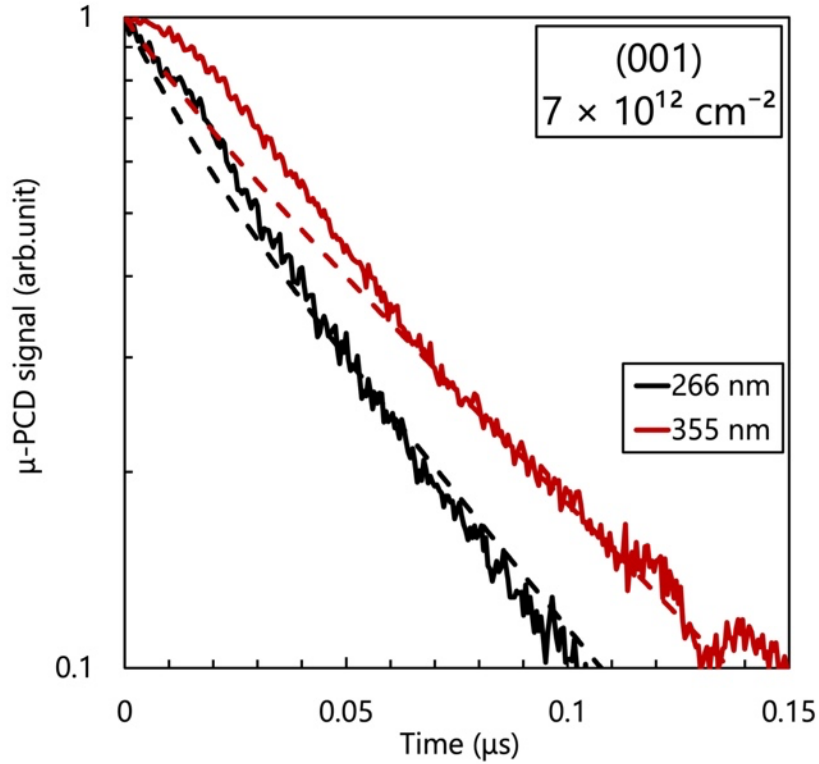
Fig. 2. μ-PCD curves excited at 266 or 355 nm on the (001) face at a low injected photon density of 7×10^{12} cm^{-2}. The solid lines represent the experimental curves, and the dotted lines represent the calculated ones with an S of 1×10^9 cm s^{-1} and τ_{bulk} of 64 ns.

Figure 3 shows μ-PCD curves of the (100) face excited at wavelengths of 266 and 355 nm at an injected photon density of 7×10^{12} cm^{-2}. Contrary to the (001) face, there was little difference between the two excitation wavelengths.
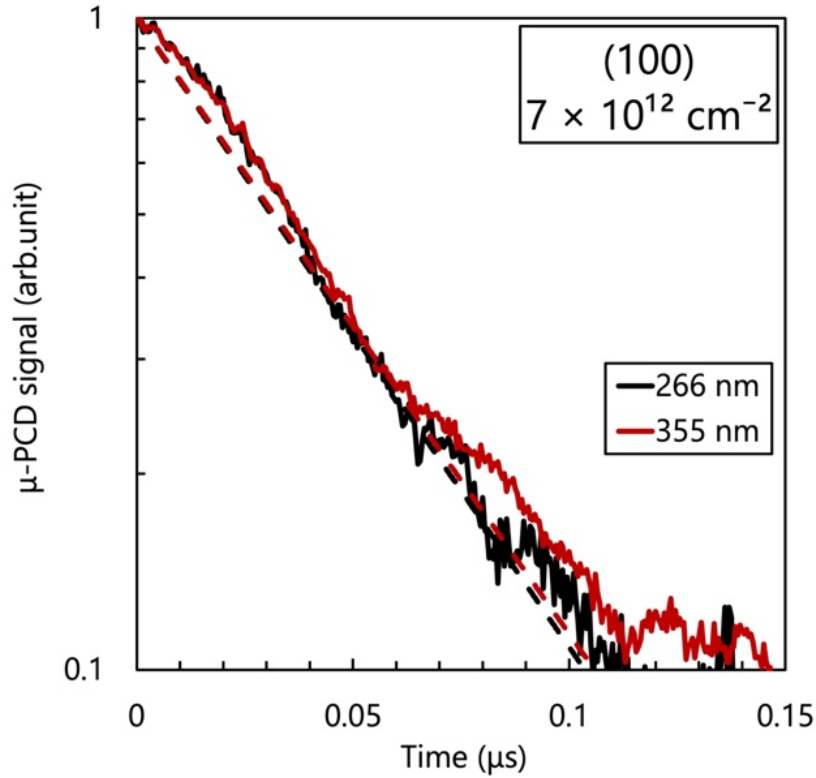
Fig. 3. μ-PCD curves excited at 266 or 355 nm on the (100) face at a low injected photon density of 7×10^{12} cm^{-2}. The solid lines represent the experimental curves, and the dotted lines represent the calculated curves with S less than 8×10^7 cm s^{-1} and τ_{bulk} of 35–46 ns.

We observed the μ-PCD curves using an injected photon density of 5×10^{14} cm^{-2}, as shown in Fig. 4 for the (001) face. Compared with Fig. 2, at the 355 nm excitation, the decay at a high injected photon density is faster than that at a low injected photon density. On the contrary, the decay curves at the 266 nm excitation were almost the same for two different injected photon densities. Additionally, we observed decay curves at various temperatures, as shown in Fig. 4, and all the decay curves were independent of temperature. This implies that the recombination centers in our samples are deep enough that will not emit carriers to the conduction or valence band at measurement temperatures [13], even though identification of the physical origin of the centers is difficult.
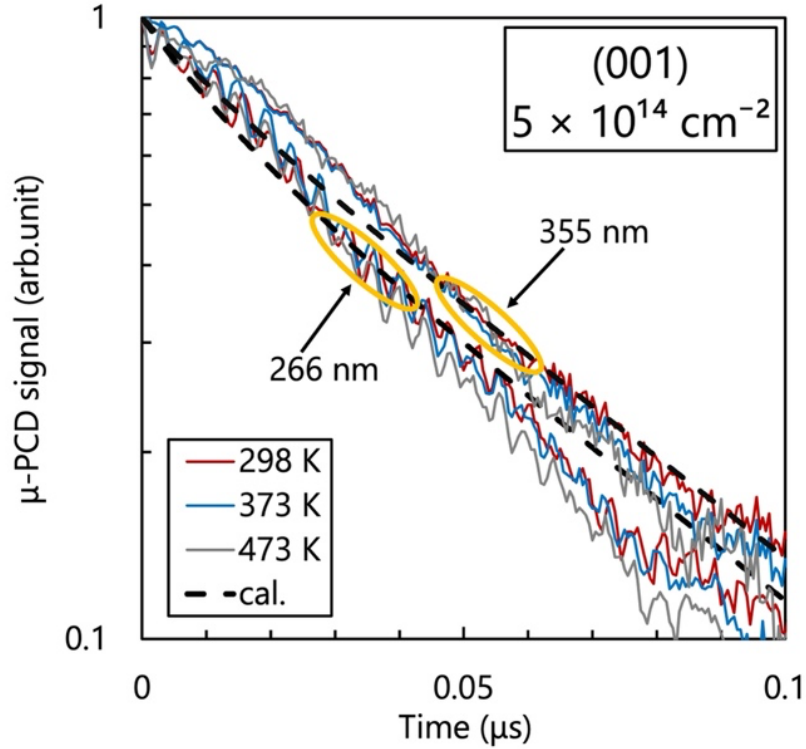
Fig. 4. Temperature dependence of the μ-PCD curves excited using the 266 and 355 nm lasers for the (001) face at a high injected photon density of 5×10^{14} cm^{-2} at temperatures of 298–473 K. The solid lines are experimental lines, and the dotted lines are calculated lines with an S of 1×10^9 cm s^{-1} and τ_{bulk} of 54 ns.

We plotted the experimental 1/e lifetime (decay time from the peak to 1/e) $\tau_{1/e}$ obtained from the μ-PCD curves against the injected photon density for the (001) and (100) crystal faces, as shown in Fig. 5. Although Auger and bimolecular recombinations have a strong dependence on the excited carrier concentration, $\tau_{1/e}$ for our samples shows a moderate dependence on the injected photon densities. Therefore, in our samples, the Auger and bimolecular recombinations were negligible. For the (001) face, $\tau_{1/e}$ for the 266 nm excitation was almost unchanged, whereas that for the 355 nm excitation, it decreased with increasing injected photon density. In contrast, for the (100) face, there was no significant difference between the two excitation wavelengths, and $\tau_{1/e}$ decreased with increasing injected photon density.
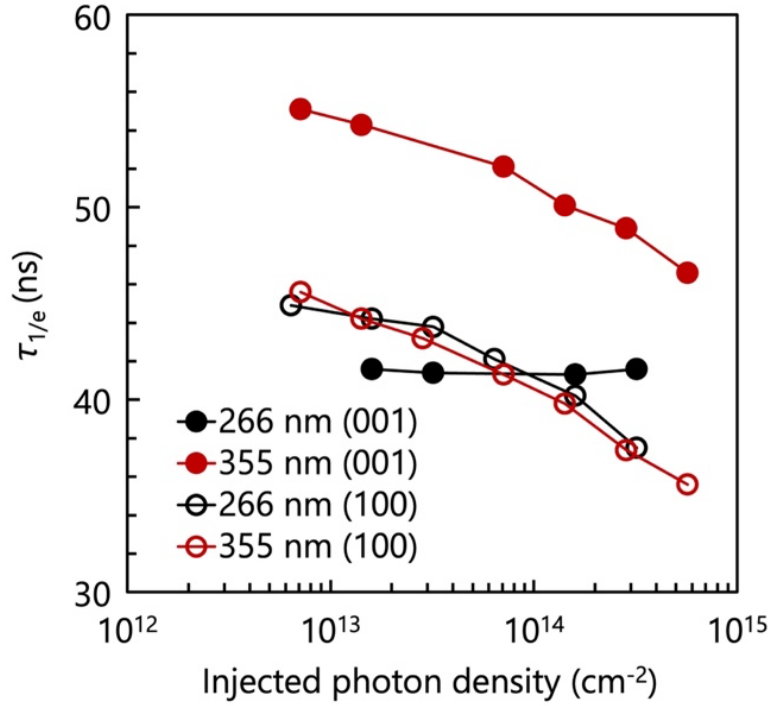
Fig. 5. Injected photon density dependence of $\tau_{1/e}$ excited at wavelengths of 266 and 355 nm on the (001) and (100) crystal faces.

We fitted the experimental $\tau_{1/e}$ with the calculated $\tau_{1/e}$ to estimate S and τ_{bulk}. The following equations were employed to calculate the excess carrier concentration [8]:

$$\frac{\partial \Delta n(x,t)}{\partial t} = D_a \frac{\partial^2 \Delta n(x,t)}{\partial x^2} - \frac{\Delta n(x,t)}{\tau_{bulk}}, \tag{1}$$

where $\Delta n(x,t)$ is the excess carrier concentration, and D_a is the ambipolar diffusion coefficient. The value of D_a is provided in [9]

$$D_a = \frac{p+n}{p/D_n + n/D_p}, \tag{2}$$

where n and p are the free-electron and free-hole concentrations, respectively. Here, we consider the samples as n-type semiconductors and set n as 2×10^{18} cm^{-3}, which is the linear average value between the minimum and maximum excess carrier concentration calculated by the injected photon densities. D_n and D_p are the diffusion constants of electrons and holes, respectively, which are estimated from

carrier mobilities μ_p and μ_n. We set $\mu_p = \mu_n = 0.02$ cm^2 V^{-1} s^{-1} [14–16]. The boundary conditions are given according to the following equations [8]:

$$D_a \frac{\partial \Delta n\,(0,t)}{\partial t} = S_0 \Delta n\,(0,t)\ and$$

$$D_a \frac{\partial \Delta n\,(W,t)}{\partial t} = -S_w \Delta n\,(W,t), \tag{3}$$

where S_0 and S_W are the surface recombination velocities at the excited and back sides of the sample, respectively, and W is the thickness of the sample. Because the thickness of the substrate was 0.05 cm, the excess carrier did not diffuse to the back side of the sample. Therefore, we set the values of S_w to 0 and W to 0.01 cm, which is deeper than the penetration depth. The initial carrier concentration profile with illumination by a light pulse is expressed as [9,8]

$$\Delta n(x,0) = g_0 \exp(-\alpha x), \tag{4}$$

where g_0 is the carrier concentration at $t = 0$ and α is the absorption coefficient corresponding to the excitation wavelengths (53 000 cm^{-1} for 266 nm and 27 000 cm^{-1} for 355 nm [17], which are reciprocal to the penetration depths). From the solution of equation (1) using D_a from equation (2) and the boundary conditions of equation (3) with the initial conditions of equation (4), we calculated $\Delta n(x,t)$. Thereafter, we obtained the time-dependent µ-PCD signals from the depth integration of the product of excess carrier concentrations and mobilities.

For the (001) face, with $S = 1 \times 10^9$ cm s^{-1} and $\tau_{bulk} = 54$ ns, we reproduced the experimental $\tau_{1/e}$ for both the 266 and 355 nm excitations at an injected photon density of 5×10^{14} cm^{-2}. In addition, when we assumed a constant S for all the injected photon densities, at 7×10^{12} cm^{-2}, we reproduced the experimental $\tau_{1/e}$ for the 355 nm excitation with a τ_{bulk} of 64 ns. For the (100) face, the experimental $\tau_{1/e}$ was dominated by SRH recombination with negligible surface recombination because of almost the same $\tau_{1/e}$ for both the 266 and 355 nm excitations. Therefore, we only estimated a maximum S

of 8×10^7 cm s^{-1} to reproduce the experimental $\tau_{1/e}$, and τ_{bulk} was in the range of 35–46 ns from the lowest to highest injected photon densities. The estimated S and τ_{bulk} values for the two crystal faces are summarized in Table 1, and the calculated decay curves using the estimated values are shown in Figs. 2–4.

We also estimated the N_r in the two samples using the estimated τ_{bulk}. The relationship between τ_{bulk} and the N_r is given by the following equation [18]:

$$\tau_{bulk} = \frac{1}{v_{th} \sigma N_r}, \tag{5}$$

where σ is the capture cross-section of the recombination center which is set at a typical value of 1×10^{-15} cm^2 [8], and v_{th} is the thermal velocity which is given by the following equation:

$$v_{th} = \sqrt{\frac{3kT}{m^*}}, \tag{6}$$

where k is the Planck constant, T is the temperature, and m^* is the effective mass of carriers and is reported as $1.04m_0$ [19]. Using equations (5) and (6), we estimated N_r as 1.4–1.7×10^{15} cm^{-3} for (001) face and 2.2–2.6×10^{15} cm^{-3} for (100) face, and also listed in Table 1.

Table 1. Estimated parameters based on the decay curves of µ-PCD

Crystal face	S (cm s^{-1})	τ_{bulk} (ns)	N_r (cm^{-3})
(001)	1×10^9	54–64	1.4–1.7×10^{15}
(100)	$< 8 \times 10^7$	35–46	2.2–2.6×10^{15}

The difference in S for the (001) and (100) faces indicates a difference in the density of the surface states owing to the atomic configurations. Although we only observed the (001) and (100) faces, we will characterize the other crystal faces in the future. We also observed a difference in τ_{bulk} and corresponding N_r between the samples. The

observed difference was of the order of 10^{15} cm^{-3}, and it means that measurements and analysis conducted in this work are effective to monitor surface recombination and slight difference in bulk quality among materials.

3.4 Conclusions

In summary, we characterized the carrier lifetimes of BiVO$_4$ single crystals with the (001) and (100) faces using the TR-PL and μ-PCD methods. The carrier lifetimes in the samples were dominated by the surface and SRH recombinations. Our estimated S and τ_{bulk} show a larger S and a longer τ_{bulk} for the sample with the (001) face compared to those for the sample with the (100) face. We believe that these quantitative S and τ_{bulk} values will be helpful for the design of BiVO$_4$ photocatalysts.

References

[1] D.K. Lee and K.-S. Choi, *Nat Energy*, **3**, 53–60 (2017).

[2] Y. Qi, J. Zhang, Y. Kong, Y. Zhao, S. Chen, D. Li, W. Liu, Y. Chen, T. Xie, J. Cui, C. Li, K. Domen, and F. Zhang, *Nat Commun*, **13**, 484 (2022).

[3] Y. Lu, Y. Yang, X. Fan, Y. Li, D. Zhou, B. Cai, L. Wang, K. Fan, and K. Zhang, *Advanced Materials*, **34**, 2108178 (2022).

[4] Y. Wang, D. Chen, J. Zhang, M. -Sadeeq (Jie Tang) Balogun, P. Wang, Y. Tong, and Y. Huang, *Adv Funct Materials*, **32**, 2112738 (2022).

[5] A. Kudo, K. Omori, and H. Kato, *J. Am. Chem. Soc.*, **121**, 11459–11467 (1999).

[6] C. Hill, M.C. Weber, J. Lehmann, T. Leinen, M. Fiebig, J. Kreisel, and M. Guennou, *APL Materials*, **8**, 081108 (2020).

[7] M. Kato, H. Najima, and T. Ozawa, *J. Electrochem. Soc.*, **166**, H468–H472 (2019).

[8] M. Kato, T. Ozawa, and Y. Ichikawa, *J. Phys. D: Appl. Phys.*, **54**, 345106 (2021).

[9] M. Kato, Z. Xinchi, K. Kohama, S. Fukaya, and M. Ichimura, *Journal of Applied Physics*, **127**, 195702 (2020).

[10] Y. Chen, X. Ma, D. Li, H. Wang, and C. Huang, *RSC Adv.*, **7**, 4395–4401 (2017).

[11] T. Asada, Y. Ichikawa, and M. Kato, *JoVE*, 59007 (2019).

[12] M. Kato and Y. Kato, *Chemical Physics Letters*, **805**, 139955 (2022).

[13] M. Kato, K. Kohama, Y. Ichikawa, and M. Ichimura, *Materials Letters*, **160**, 397–399 (2015).

[14] M. Ziwritsch, S. Müller, H. Hempel, T. Unold, F.F. Abdi, R. Van De Krol, D. Friedrich, and R. Eichberger, *ACS Energy Lett.*, **1**, 888–894 (2016).

[15] T. Liu, M. Cui, and M. Dupuis, *J. Phys. Chem. C*, **124**, 23038–23044 (2020).

[16] F.F. Abdi and S.P. Berglund, *J. Phys. D: Appl. Phys.*, **50**, 193002 (2017).

[17] T. Hayashi, K. Asano, J. Suda, and T. Kimoto, *Journal of Applied Physics*, **109**, 014505 (2011).

[18] I. Abdellaoui, M.M. Islam, M. Remeika, Y. Higuchi, T. Kawaguchi, T. Harada, C. Budich, T. Maeda, T. Wada, S. Ikeda, and T. Sakurai, *J. Phys. Chem. C*, **124**, 3962–3972 (2020).

[19] Z. Zhao, Z. Li, and Z. Zou, *Phys. Chem. Chem. Phys.*, **13**, 4746 (2011).

Chapter 4

Effect of dislocations on carrier recombination and photoelectrochemical activity in polished and unpolished TiO₂ and SrTiO₃ crystals

4.1 Introduction

Titanium oxide (TiO₂) is one of the most widely investigated photocatalyst materials [1–6] with a band gap of 3.2 eV for the anatase structure and 3.0 eV for the rutile structure. Strontium titanate (SrTiO₃) is a cubic perovskite oxide with a band gap of 3.2 eV and exhibits promising photocatalytic activity in water-splitting reactions [7–11].

In recent years, performance improvement of TiO₂ and SrTiO₃ has been widely researched. However, the crystal defect significance in these materials remains insufficiently understood. Dislocation is one of the crystal defects that can be It can be easily generated during material preparation. As mentioned in Ch. 3, the defect influences the charge carrier lifetime and then influences the photocatalytic activity and performance [12]. Therefore, we investigate the effect of dislocation on the carrier lifetime and the photocatalytic performance of TiO₂ and SrTiO₃.

Chemical-mechanical polishing (CMP) is widely used to reduce the roughness and enhance the flatness or quality of the surface of a material in semiconductor processing. Through the CMP process, the initial defects, such as scratches and pits [13,14], fall-on particles [14], and crystalline inclusions [15], can be effectively eliminated. Therefore, we consider that CMP can also effectively reduce surface dislocations in materials.

In this chapter, we consider that the dislocation can be present in the material without CMP treatment, and it will increase the carrier lifetime and improve the photoelectrochemical performance. Therefore, we adopt single-sided CMP-treated TiO₂ and SrTiO₃ single crystals to characterize carrier lifetime using μ-PCD method

and photocurrent in both unpolished and polished faces.

4.2 Material and methods

Commercial undoped and Nb-0.01 wt % doped TiO$_2$ with (001) face and SrTiO$_3$ with (100) face single crystals 10 × 10 × 0.5 mm^3 in size (Crystal Base Co., Ltd.) were characterized. All samples were grown using the Verneuil method, however, for the doped samples, niobium (Nb) was intentionally added during crystal growth. The doping concentration is 0.01 wt% (weight percent). The samples were single-side polished using chemical–mechanical polishing (CMP). During the polishing process, the single crystals formed on the substrates undergo initial rough polishing to achieve a certain level of surface smoothness. Subsequently, CMP is employed to further polish the TiO$_2$ and SrTiO$_3$ crystals on the polished faces, reducing their roughness. Colloidal silica is typically used as the polishing agent in CMP. On the other hand, for the unpolished faces, rough polishing is performed to align them parallel to the polished faces after being cut. CMP is not applied to these unpolished faces. The roughness measured using a white light confocal microscope (OPTELICS HYBRID C3, Lasertec Corporation) of the unpolished and polished faces is 0.65 and 0.05 μm, respectively.

A custom setup discussed in detail in a previous report [16] was used for μ-PCD measurements. Yttrium aluminum garnet (YAG) lasers with wavelengths of 266 and 355 nm and pulse width of 1 ns were used as excitation light sources (FTSS 266–200 and FTSS 355–50, CryLas) [17–21]. The spot size [20] of the two lasers was 0.13 cm$^-$^{2}. The laser intensity was 0.06–0.6 mW for the 266 nm laser and 0.2–4.0 mW for the 355 nm laser. The injected photon density was set to 1.1×10^{13}–1.1×10^{14} cm^{-2} for the 266 nm wavelength and 2.8×10^{13}–5.7×10^{14} cm^{-2} for the 355 nm wavelength. For μ-PCD measurements, microwaves generated by a Gunn diode at a frequency of 10 GHz were irradiated through the waveguide to the unexcited side of the sample and used as a measurement probe [19,20]. The reflected microwaves were detected using a Schottky barrier diode, and the intensity of the reflected microwaves was converted to a voltage signal for μ-PCD measurements [18]. To reduce the influence of the sample

conductivity, we normalized the original signal from the peak in the carrier recombination observation. XPS was performed using PHI Quantes (ULVAC-PHI, Inc.). TEM images were obtained using a JEM-ARM200F microscope (JEOL Ltd). To measure the photocurrent, we used a three-electrode PEC system [12,22–24]; the Nb-doped TiO$_2$ or SrTiO$_3$ was the working electrode, a platinum (Pt) plate acted as the counter electrode, and Ag/AgCl was the reference electrode. We formed aluminum (Al) ohmic contacts [12,22] on Nb-doped samples to behave as photoelectrodes. Hydrochloric acid (1 M) was used as the electrolyte. The irradiation light intensity was set to 0.1 W/cm^{-2} using a solar simulator (LH-10500, Abet Technologies, Inc.). The potential range was –0.5–1.0 V vs Ag/AgCl and was controlled and measured using function generator (HB-305) combined with a potentiostat/galvanostat (HA-151B, HOKUTO DENKO CORPORATION).

4.3 Results and discussion

The μ-PCD curves as a function of injected photon density for the undoped TiO$_2$ single crystal excited by 266 nm and 355 nm lasers at room temperature are shown in Fig. 1. The unpolished face [Fig. 1(a) and (c)] shows obvious fast decay and slow decay, whereas the CMP-processed face [Fig. 1 (b) and (d)] shows only fast decay. Generally, the recombination center at deep levels represents fast decay, and the slow decay of charge carriers is caused by the trapping of minority carriers at the defect level [25]. Therefore, recombination centers dominate the carrier recombination for the polished face, whereas traps are present in the unpolished face. Moreover, the μ-PCD curves of the unpolished face show slight injected photon density dependence, while those of the polished face show no injected photon density dependence. This indicates that the carrier recombination of the unpolished face is dominated by the Shockley–Read–Hall (SRH) recombination [20], while that of the polished face is dominated by the sufficiently fast recombination at the bulk recombination center which is similar to SrTiO$_3$ [18,26]. In addition, the Auger and bimolecular recombination which strongly depend on charge carrier concentration are negligible [19,21].

48
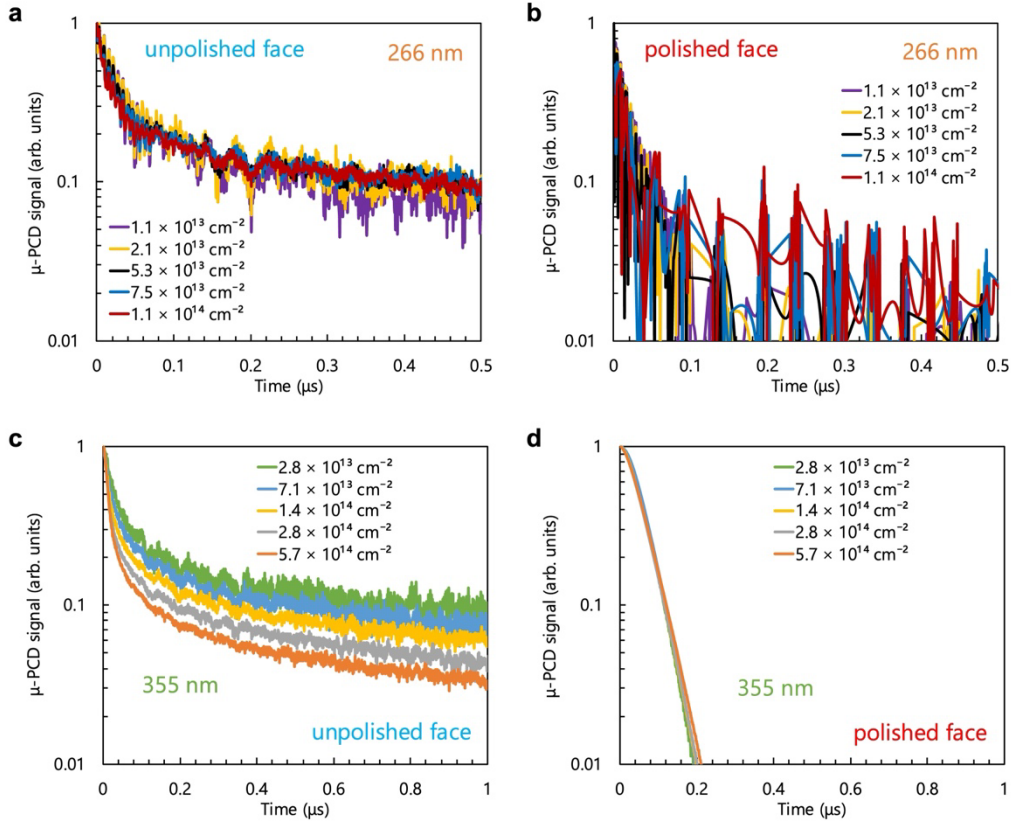
Fig. 1. Injected photon density dependence of μ-PCD curves of TiO₂ for (a) unpolished face, (b) polished face, and (c) unpolished face, (d) polished face excited by a 355 nm laser.

The temperature dependence of μ-PCD curves for undoped TiO₂ and SrTiO₃ single crystals excited by the 355 nm laser at an injected photon density of 5.7×10^{14} cm^{-2} is shown in Fig. 2. For TiO₂, the decay curves of the unpolished face [Fig. 2(a)] show significant temperature dependence, while those of the polished face [Fig. 2(b)] are independent of temperature. For unpolished TiO₂, increasing the temperature lowers the rate of μ-PCD. Generally, in Shockley-Read-Hall (SRH) recombination, the slower decay with increasing temperature can be explained by an increase in the rate of carrier emission from recombination centers [27] in the unpolished TiO₂ face. The polished TiO₂ face has recombination centers that are deep enough that the carriers will not be emitted to the valence band or conduction band at the experimental temperatures [17,20]. For SrTiO₃, the decay curves of both the unpolished [Fig. 2(c)] and polished

49

faces [Fig. 2(d)] show temperature dependence, which is similar to our previous report [18]. Moreover, the μ-PCD of SrTiO$_3$ increased with increasing temperature, which can be explained by the increase in the thermal velocity of the carriers or the increase in the capture cross-section of traps or recombination centers with increasing temperature [18].
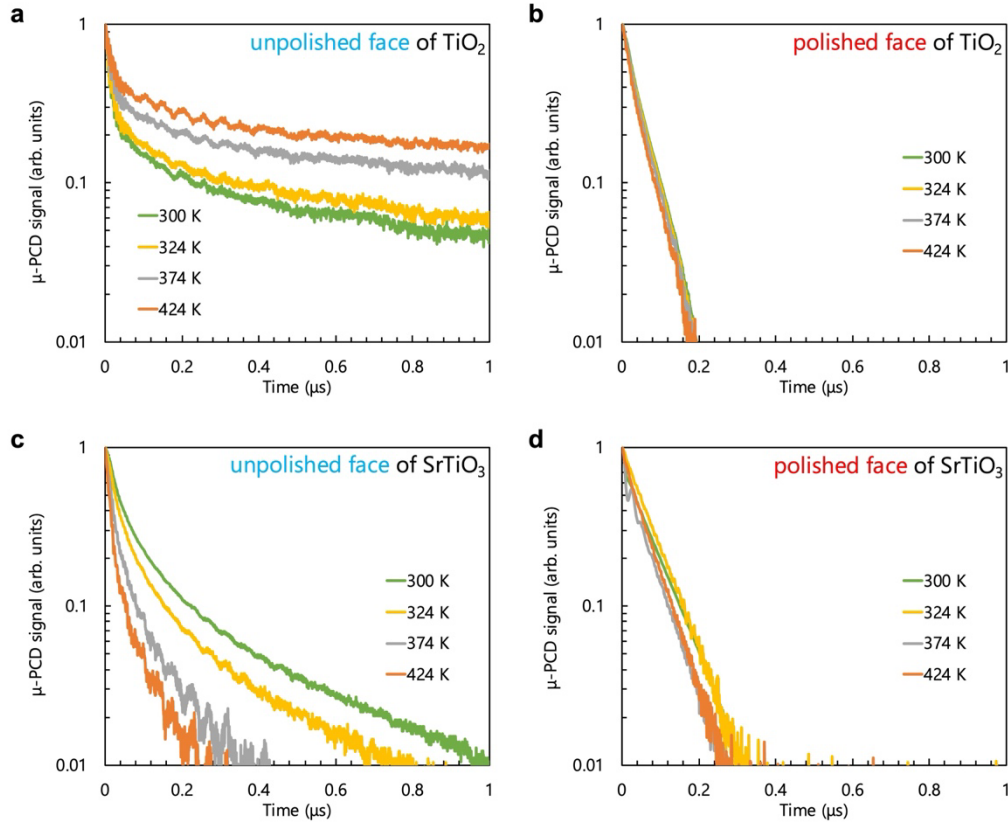
Fig. 2. Temperature dependence of μ-PCD curves of samples excited by a 355 nm laser at an injected photon density of 5.7×10^{14} cm^{-2} for (a) unpolished TiO$_2$ face, (b) polished TiO$_2$ face, (c) unpolished SrTiO$_3$ face, and (d) polished SrTiO$_3$ face.

The constituent elements and electronic states of Ti 2p and O 1s for TiO$_2$ and SrTiO$_3$ on both the polished and unpolished faces were observed by X-ray photoelectron spectroscopy (XPS) measurements. The peak positions of Ti 2p for the unpolished and polished faces of TiO$_2$ and SrTiO$_3$ did not change. When observing the O 1s peaks for TiO$_2$ [Fig. 3(a)], there is no significant difference in the XPS spectra between the two faces. The peaks at binding energies 529.4 eV are attributed to lattice oxygen, while the shoulder peaks at 531.4 eV are attributed to oxygen vacancy [28]. Moreover, the

intensity of the main peaks and shoulder peaks are almost the same for both unpolished and polished faces, respectively. It indicates that the chemical status of oxygen in the two faces is the same. However, for SrTiO₃ [Fig. 3(b)], the peak on the unpolished face is more significant than that on the polished face at a binding energy of 531.4 eV. The peaks at 528.8 eV are associated with the O^{2-} ions in the crystal structure of SrTiO₃, and the middle peak at around 531.4 eV, is attributed to O^{2-} in the oxygen vacancy of SrTiO₃ surface [29–31], or a surface-absorbed hydroxyl group [32–34]. Furthermore, the peak intensity of the unpolished face at 528.8 eV is significantly lower than that of the polished face. It implies that the ratio of oxygen vacancies, which has a low formation energy [77], or the hydroxyl on unpolished faces is higher than on polished faces.
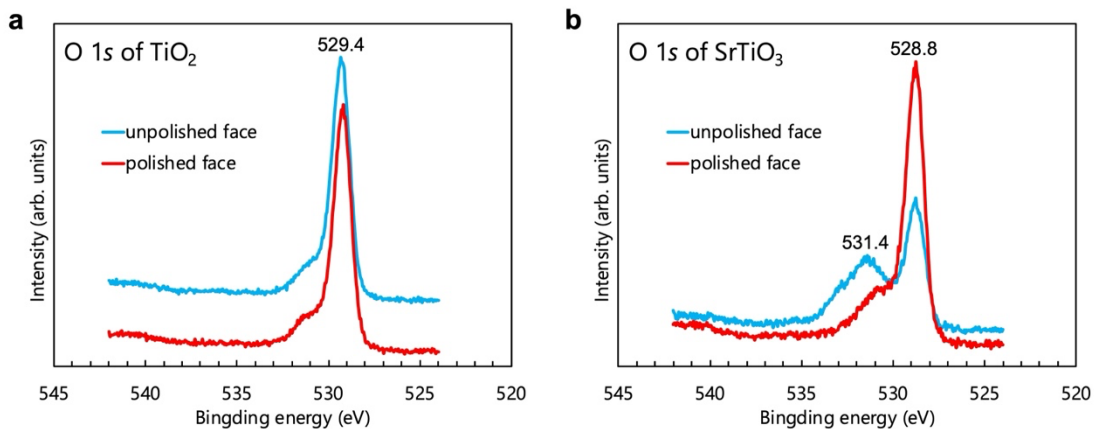
Fig. 3. The O 1*s* XPS spectra of (a) TiO₂ and (b) SrTiO₃ for both polished and unpolished faces.

Transmission electron microscopy (TEM) was employed to confirm the structure of the polished and unpolished surfaces of both materials. Prior to TEM, the samples were processed by a focused ion beam (FIB) to a maximum cross-section depth of 10 μm for the cross-sectional TEM observation. To check for surface defects, we did Pt sputtering directly. The cross-sectional TEM images near the surface are shown in Fig. 4 and no clear contrasts are observed between the polished faces of TiO₂ [Fig. 4(b)] and SrTiO₃ [Fig. 3(d)]. For the unpolished TiO₂ face [Fig. 4(a)], linear contrasts were observed, suggesting the presence of dislocations. The dislocation lines were measured to be at

approximately 55° in the [001] direction. This angle was the closest to 57.2° between

the [10$\bar{1}$] or equivalent [$\bar{1}$01] and [001] directions in rutile TiO$_2$ single crystals [35].

Therefore, the possible direction of these dislocations can be considered to be in the

[10$\bar{1}$] or [$\bar{1}$01] direction. For the unpolished SrTiO$_3$ face [Fig. 4(c)], contrasts were also

observed; some of the dislocations existed in the direction parallel to the [110] direction,

and the dislocation lines existed in the [010] direction, which is approximately 45° from

the [110] direction. It has been reported that excess oxygen vacancies in the crystal tend

to accumulate due to the low formation energy of oxygen vacancies near dislocations

[36] in SrTiO$_3$. Therefore, according to the XPS results, oxygen defects are probably

present near the dislocations. It has been reported that ⟨100⟩{011} edge dislocations in

SrTiO$_3$ can accumulate high concentrations of positively charged oxygen vacancies in

their core [37]. It further implies that edge dislocation defects can extend into the bulk.

Additionally, the difference between SrTiO$_3$ and TiO$_2$ defect networks is the crystalline

structure. SrTiO$_3$ is a cubic structure, while TiO$_2$ is a rutile structure.
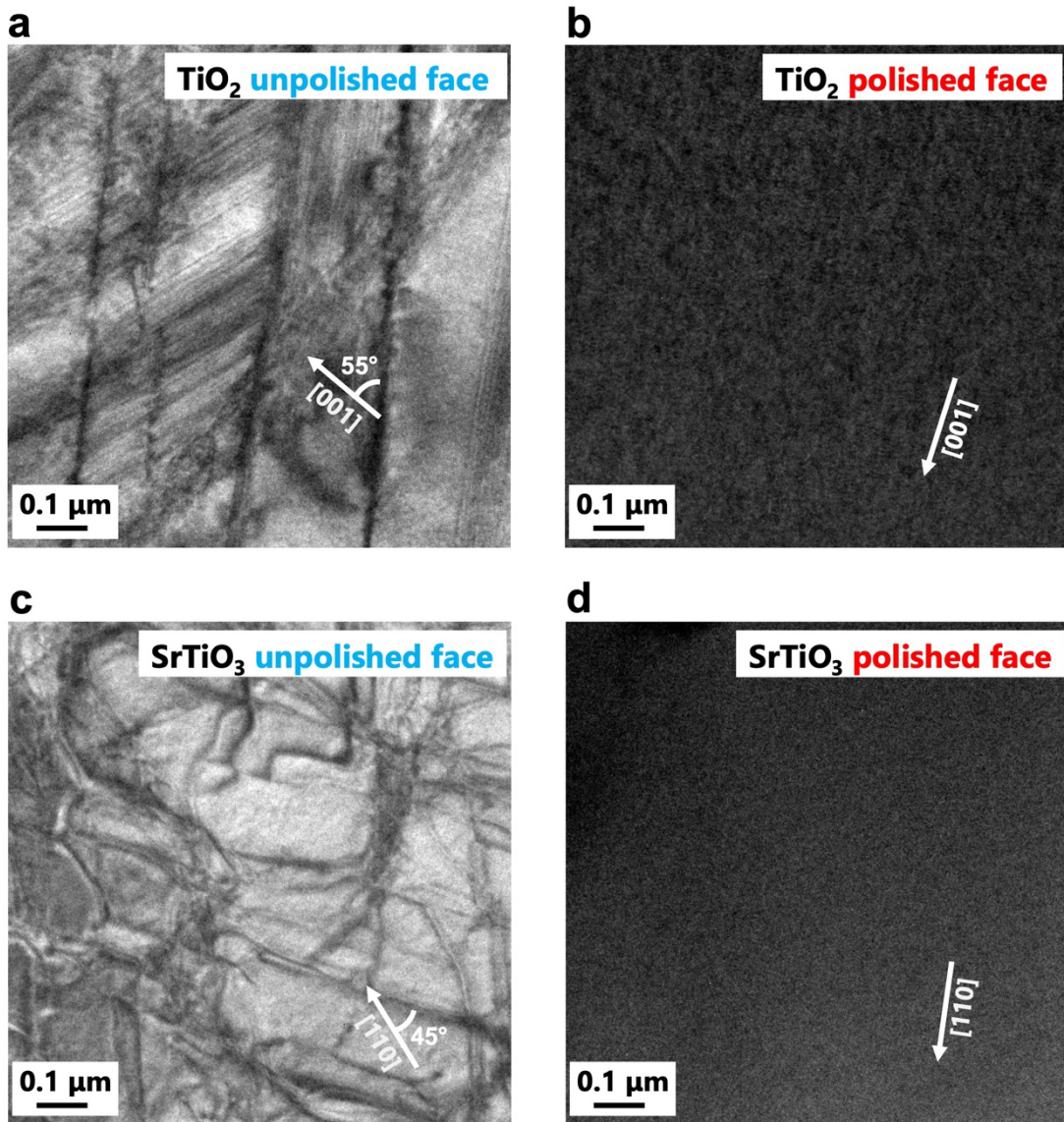
Fig. 4. TEM micrographs of (a) unpolished TiO₂ face, (b) polished TiO₂ face, (c) unpolished SrTiO₃ face, and (d) polished SrTiO₃ face. All samples were obtained by FIB processing.

To analyze the effect of dislocations on PEC activity, we measured the photocurrent (Fig. 5) in the unpolished and polished faces under an irradiated light intensity of 0.1 W/cm^2. Nb-doped TiO₂ [12,22,38] and SrTiO₃ [18,38] show excellent performance in photoelectrochemical water splitting. Therefore, we used Nb-doped TiO₂ and SrTiO₃ whose crystal faces are the same as the undoped ones, instead of undoped ones, which do not conduct. For Nb-doped TiO₂ [Fig. 5(a)], the maximum photocurrent of the unpolished face was one-third 1/3 of the polished face, whereas, for Nb-doped SrTiO₃

[Fig. 5(b)], the maximum photocurrent of the unpolished face was two-thirds 2/3 of the polished face. Moreover, the on-site potential of the polished face was more negative than that of the unpolished face for both samples. Therefore, the unpolished faces showed smaller photocurrents than those for the polished faces for both materials.
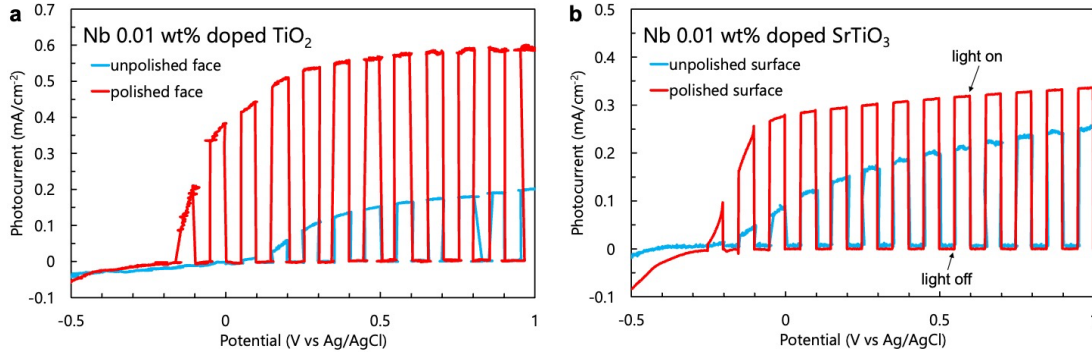
Fig. 5. Photocurrents generated by unpolished and polished faces for 0.01 wt% Nb-doped (a) TiO₂ and (b) SrTiO₃ at an irradiated light intensity of 0.1 W/cm².

4.4 Conclusion

In summary, our observations revealed that μ-PCD curves exhibited a clear slow decay for the unpolished faces of both TiO₂ and SrTiO₃ single crystals, indicating the presence of traps in these faces compared with the polished faces. The sensitivity of the μ-PCD curves to the injected photon density differed between the unpolished and polished faces, suggesting that charge carrier recombination predominantly occurred through SRH recombination with the influence of minority carrier trap filling in the unpolished face. The insensitivity of the polished face to temperature can be attributed to deep recombination centers. Furthermore, the opposite temperature dependences observed for the unpolished TiO₂ and SrTiO₃ faces indicate that carrier recombination is induced by different mechanisms in the recombination centers of these two materials. The XPS analysis revealed a high concentration of oxygen vacancies in the unpolished SrTiO₃ face, indicating the presence of oxygen defects or hydroxyl. Consistent with the temperature dependence of μ-PCD results for unpolished faces, these oxygen defects which serve as carrier recombination centers in SrTiO₃ contribute to different

recombination mechanisms compared to TiO$_2$. The TEM images confirm the presence of dislocations in the unpolished faces of both materials. These dislocations created minority carrier traps in the unpolished faces, inducing the slow decay observed in the measurements. Moreover, dislocations can create oxygen defects in SrTiO$_3$. In addition, a higher photocurrent was observed in the unpolished faces than in the polished faces for both materials. The roughness values for the unpolished and polished faces were measured as 0.65 μm and 0.05 μm, respectively. Considering the significantly rougher surface, which increases the contact area with the electrolyte and enhances the light confinement effect, and the apparent increase in carrier lifetime caused by the traps in the unpolished face, it was expected that the photocurrent in the unpolished faces will be higher than that in the polished faces. However, the unpolished face did not have a positive effect on PEC activity. These contrasting results clearly indicate that dislocations have a detrimental impact on the PEC activity, even in the case of TiO$_2$ and SrTiO$_3$, which are considered to be the most typical photocatalysts for water splitting. Therefore, it is essential to utilize a surface without dislocations to improve the performance of PEC water splitting. Even for powders or nanoscale particles, material preparation processes that do not induce dislocations are required to achieve efficient photocatalytic performance. One approach is suggested to soften the surface of the sample through an excellent polishing process, which helps improve the crystalline quality. These findings will significantly contribute to the development of more efficient processes for photocatalysis.

References

[1] Q. Guo, C. Zhou, Z. Ma, and X. Yang, *Adv. Mater.*, **31**, 1901997 (2019).

[2] A. Meng, L. Zhang, B. Cheng, and J. Yu, *Adv. Mater.*, 1807660 (2019).

[3] K. Nakata and A. Fujishima, *Journal of Photochemistry and Photobiology C: Photochemistry Reviews*, **13**, 169–189 (2012).

[4] K. Ishibashi, A. Fujishima, T. Watanabe, and K. Hashimoto, *Journal of Photochemistry and Photobiology A: Chemistry*, **134**, 139–142 (2000).

[5] K. Nakata, T. Ochiai, T. Murakami, and A. Fujishima, *Electrochimica Acta*, **84**, 103–111 (2012).

[6] M.R. Al-Mamun, S. Kader, M.S. Islam, and M.Z.H. Khan, *Journal of Environmental Chemical Engineering*, **7**, 103248 (2019).

[7] K. Iwashina and A. Kudo, *J. Am. Chem. Soc.*, **133**, 13272–13275 (2011).

[8] H. Kato and A. Kudo, *J. Phys. Chem. B*, **106**, 5029–5034 (2002).

[9] S. Ouyang, H. Tong, N. Umezawa, J. Cao, P. Li, Y. Bi, Y. Zhang, and J. Ye, *J. Am. Chem. Soc.*, **134**, 1974–1977 (2012).

[10]R. Konta, T. Ishii, H. Kato, and A. Kudo, *J. Phys. Chem. B*, **108**, 8992–8995 (2004).

[11]T. Ishii, H. Kato, and A. Kudo, *Journal of Photochemistry and Photobiology A: Chemistry*, **163**, 181–186 (2004).

[12]M. Kato, H. Najima, and T. Ozawa, *J. Electrochem. Soc.*, **166**, H468–H472 (2019).

[13]G. Pan, Y. Zhou, G. Luo, X. Shi, C. Zou, and H. Gong, *J Mater Sci: Mater Electron*, **24**, 5040–5047 (2013).

[14]H.K. Hsu, T.C. Tsai, C.W. Hsu, W. Lin, R.P. Huang, C.L. Yang, and J.Y. Wu, *Microelectronic Engineering*, **112**, 121–125 (2013).

[15]H. Landis, P. Burke, W. Cote, W. Hill, C. Hoffman, C. Kaanta, C. Koburger, W. Lange, M. Leach, and S. Luce, *Thin Solid Films*, **220**, 1–7 (1992).

[16]T. Asada, Y. Ichikawa, and M. Kato, *JoVE*, 59007 (2019).

[17]M. Kato, K. Kohama, Y. Ichikawa, and M. Ichimura, *Materials Letters*, **160**, 397–399 (2015).

[18]M. Kato, T. Ozawa, and Y. Ichikawa, *J. Phys. D: Appl. Phys.*, **54**, 345106 (2021).

[19]M. Kato, Z. Xinchi, K. Kohama, S. Fukaya, and M. Ichimura, *Journal of Applied Physics*, **127**, 195702 (2020).

[20]E. Zhang and M. Kato, *J. Phys. D: Appl. Phys.*, **56**, 025103 (2023).

[21]K. Tanaka, K. Nagaya, and M. Kato, *Jpn. J. Appl. Phys.*, **62**, SC1017 (2023).

[22]E. Zhang, Z. Liu, and M. Kato, *Solar Energy Materials and Solar Cells*, **230**,

111260 (2021).

[23] M. Kato, K. Miyake, T. Yasuda, M. Ichimura, T. Hatayama, and T. Ohshima, *Jpn. J. Appl. Phys.*, **55**, 01AC02 (2016).

[24] M. Kato and T. Ambe, *Appl. Phys. Express*, **13**, 026506 (2020).

[25] M. Kato, T. Asada, T. Maeda, K. Ito, K. Tomita, T. Narita, and T. Kachi, *Journal of Applied Physics*, **129**, 115701 (2021).

[26] M. Kato and Y. Kato, *Chemical Physics Letters*, **805**, 139955 (2022).

[27] T. Hayashi, K. Asano, J. Suda, and T. Kimoto, *Journal of Applied Physics*, **109**, 014505 (2011).

[28] B. Bharti, S. Kumar, H.-N. Lee, and R. Kumar, *Sci Rep*, **6**, 32355 (2016).

[29] H. Tan, Z. Zhao, W. Zhu, E.N. Coker, B. Li, M. Zheng, W. Yu, H. Fan, and Z. Sun, *ACS Appl. Mater. Interfaces*, **6**, 19184–19190 (2014).

[30] Y. Guo, H.M. Zeeshan, M. Yan, W. Qin, W. Yang, S. Cao, Y. Dedkov, and E. Voloshina, *Adv Energy and Sustain Res*, **4**, 2300136 (2023).

[31] J. Zhao, C. Liu, J. Li, R. Wu, J. Wang, H. Qian, H. Guo, J. Li, and K. Ibrahim, *AIP Advances*, **9**, 055208 (2019).

[32] A. Ahmed, A.M. Ahmed, A.A. Abdel-Khaliek, M. Shaban, A.A.A. Abdelazeez, and M. Rabia, *International Journal of Energy Research*, **2023**, 1–10 (2023).

[33] R. Li, T. Takata, B. Zhang, C. Feng, Q. Wu, C. Cui, Z. Zhang, K. Domen, and Y. Li, *Angew Chem Int Ed*, **62**, e202313537 (2023).

[34] H. Idriss, *Surface Science*, **712**, 121894 (2021).

[35] H. Nörenberg, F. Dinelli, and G.A.D. Briggs, *Surface Science*, **446**, L83–L88 (2000).

[36] P. Wang, W. Yi, J. Chen, S. Ito, C. Cui, and T. Sekiguchi, *J. Phys. D: Appl. Phys.*, **52**, 475103 (2019).

[37] K.K. Adepalli, J. Yang, J. Maier, H.L. Tuller, and B. Yildiz, *Adv Funct Materials*, **27**, 1700243 (2017).

[38] Y. Yang, K. Lee, Y. Kado, and P. Schmuki, *Electrochemistry Communications*, **17**, 56–59 (2012).

Chapter 5

Analysis of defects dominating carrier recombination in CeO₂ single crystal for photocatalytic applications

5.1 Introduction

Cerium oxide (CeO₂) has been extensively studied as a compelling semiconductor, and diverse methodologies have been employed to enhance its performance in CO or CO₂ reduction, photoelectrocatalytic, and heterogeneous catalytic applications [1–3] owing to its fluorite structure and a wide band gap of 3.2 eV [4–6]. As mentioned in Ch. 1, various methods are developed to synthesize CeO₂ nanoparticles. However, the impact of defects on the properties of CeO₂ has not been comprehensively elucidated for samples prepared using these synthetic methods.

As mentioned in Ch. 3 and 4, defects can directly dominate carrier recombination, thereby affecting the energy conversion efficiency [7]. Therefore, we use a high-quality single crystal synthesized using an arc furnace in this study.

In this chapter, we consider that the present defect is not single. We use TR-PL and μ-PCD methods to characterize the carrier lifetime in CeO₂. Moreover, the PL spectra measurement is used to investigate the emission region. Then, we estimate the defect level, E_T, and electron capture cross-section, σ_n, to quantitatively analyze the present defect by fitting the obtained TR-PL decay curves using rate equations.

5.2 Material and methods

Commercial undoped CeO₂ with (100) face single crystal of size $10 \times 10 \times 0.5$ mm³ was used as the sample. To characterize this sample, PL, TR-PL, and μ-PCD measurements were conducted. Yttrium aluminium garnet lasers with a wavelength of 355 nm and a pulse width of 1 ns were used as the excitation light sources. The spot

size of both lasers was 0.13 cm^2. The laser intensity was 4.0 mW, frequency was 100 Hz, corresponding injected photon density was 5.7×10^{14} cm^{-2}, and penetration depth of CeO$_2$ was ~200 nm for the 355 nm lasers [8]. For the PL and TR-PL measurements, we used a multichannel spectrometer and a photomultiplier as the detector, respectively. A long-pass filter (w/ o 565 BPF) with a cut-off wavelength of 355 nm was placed in front of the multichannel spectrometer or photomultiplier [9–13]. To measure the TR-PL separately, a 565 nm (2.19 eV) band-pass filter (w/ 565 BPF) with a centre wavelength of 565 nm and a peak transmission width of 133 nm (498.5–631.5 nm, 1.96–2.49 eV) was positioned between the 355 nm long-pass filer and the photomultiplier. For the μ-PCD measurements, a custom setup described in detail in a previous report was used [14]. Microwaves generated by a Gunn diode at a frequency of 10 GHz with an output power of 50 mW were irradiated through a waveguide on the unexcited side of the sample as a measurement probe [9,10,15–17]. Moreover, the reflected microwaves were detected using a Schottky barrier diode, and the intensity of the reflected microwaves was converted into a voltage signal for μ-PCD measurements. We normalized the signal by the peak to avoid multiple factors from impacting the TR-PL and μ-PCD measurements.

5.3 Results and discussion

Figure 1 shows the temperature-dependent PL spectra of the CeO$_2$ single crystal. Notably, no luminescence originating between the band edges is discernible even at room temperature. Instead, four prominent peaks are evident: two within the visible light region at 2.01 eV and 2.16 eV and two within the infrared region at 1.41 eV and 1.52 eV. Several works reported the peaks of PL spectra around 2.0 eV in the visible light region [18,19] and 1.62 eV in the infrared region [20] which are similar to our results. Additionally, dependence on the injected photon density is not discernible in both μ-PCD and TR-PL decay curves, regardless of whether excitation occurs at a wavelength of 266 nm or 355 nm. This observation strongly suggests that the Auger recombination process, which is highly contingent on the excess carrier concentration,

is of negligible significance [7,10,16,21]. As the temperature is increased to 423 K, the intensities of the peaks in the visible light region rapidly decrease, whereas those of the peaks in the infrared region remain comparatively stable. At 523 K, all peaks vanish. Importantly, the positions of these peaks remain consistent across all temperatures, indicating the presence of defects within the material that serve as radiative recombination centers, thereby dominating charge carrier recombination.
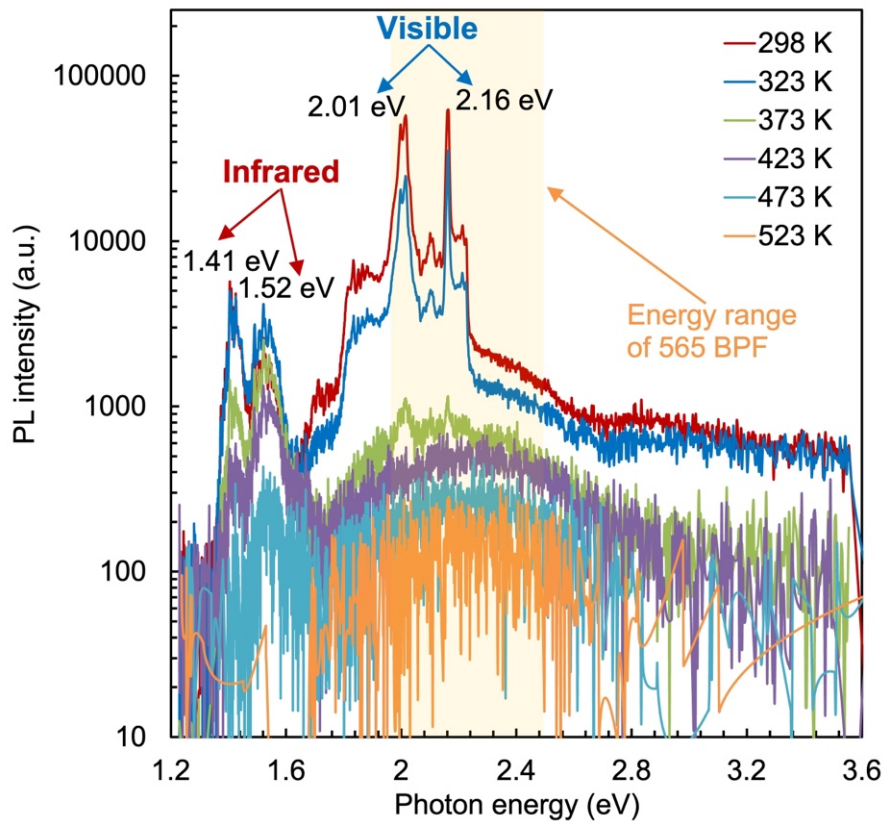
Fig. 1. Temperature dependence of PL spectra of CeO$_2$ single crystal. Light yellow part shows energy range of the 565 nm BPF.

Figure 2 shows the temperature dependence of the µ-PCD curves of the CeO$_2$ single crystal for the components with time constants shorter than 1 µs in the form of semi-logarithmic plots. As shown in this figure, the signal-to-noise ratio for µ-PCD curves is not good, however, the slight temperature dependence can be observed that as the temperature increases, the decay curves increase in speed. Therefore, we decided to adopt the TR-PL method for further discussion.
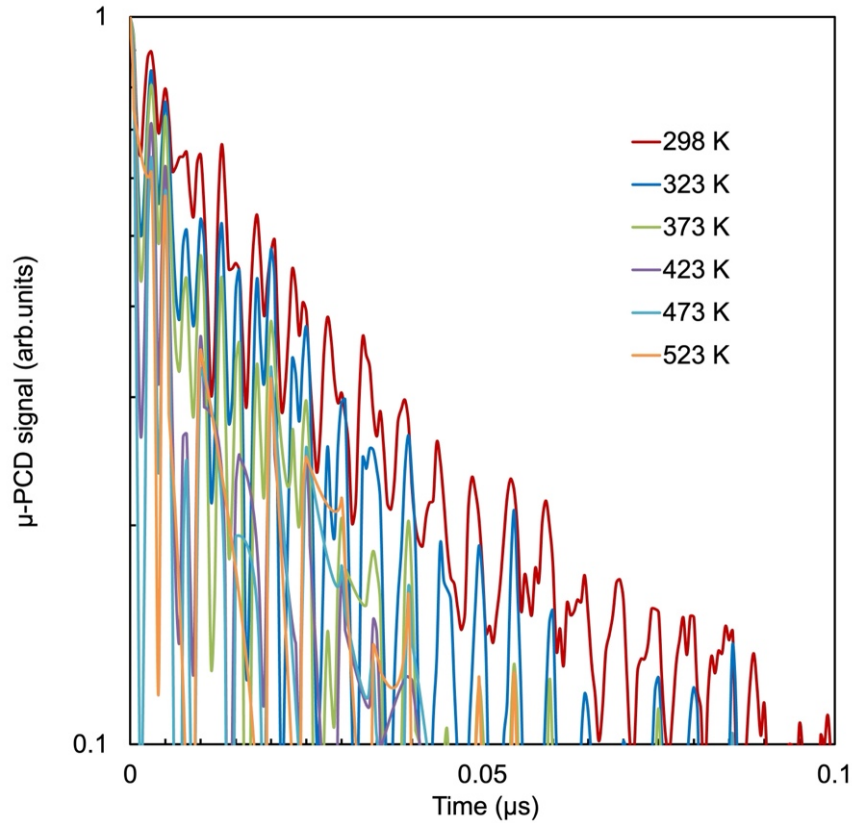
Fig. 2. Temperature dependence of μ-PCD cures of CeO$_2$ single crystal.

Figure 3 shows the temperature dependence of the TR-PL decay curves of the CeO$_2$ single crystal for the components with time constants longer than 1 μs in the form of double-logarithmic plots. As the temperature increases, the decay curves increase in speed in both w/ o 565 BPF [Fig. 3(a)] and w/ 565 BPF [Fig. 3(b)] cases. At temperatures below 323 K, the w/ o and w/ 565 BPF curves are not noticeably different. In contrast, at higher temperatures, the decay of the w/ 565 BPF curves is faster and the intensity is lower than those of the w/ o 565 BPF curves.
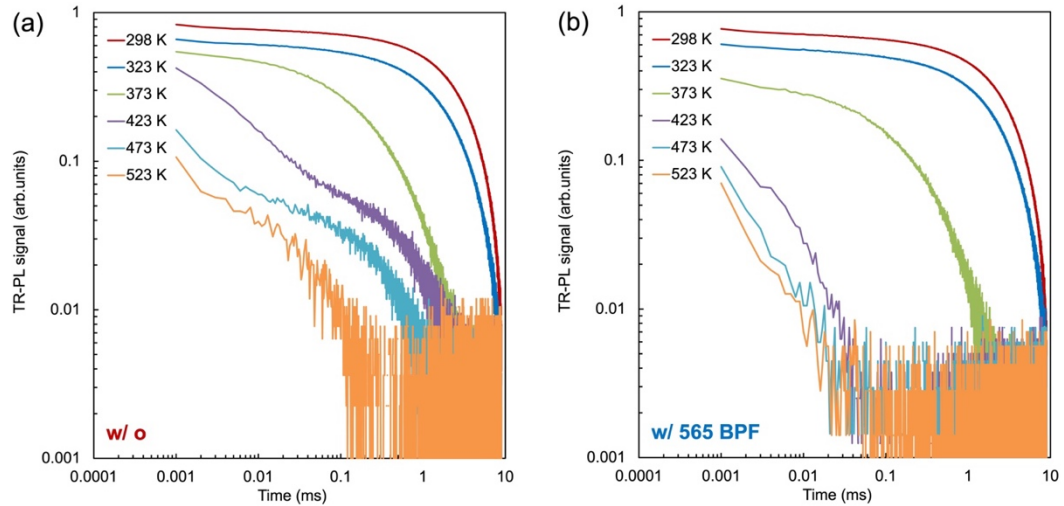
Fig. 3. Temperature dependence of TR-PL decay curves of CeO$_2$ single crystal (a) w/
o and (b) w/ 565 BPF as double-logarithmic plots.

In Fig. 4, the time constants extracted from the decay curves in Fig. 3 are plotted
against the temperature. The temperature-dependent time constants of the decay of the
w/ o 565 BPF curves are shown in Fig. 4(a). When the temperature is below 473 K, the
time constant decreases inconspicuously, whereas when the temperature exceeds 473
K, it decreases significantly. For the w/ 565 BPF curves [Fig. 4(b)], the time constants
in the visible light region are shorter than those at higher temperatures. The shorter time
constants and smaller signals of the w/ 565 BPD curves than those of the w/ o BPF
curves indicate that the full-spectrum measurement results corresponding to Figs. 3(a)
and 4(a) are dominated by the luminescence in the infrared region (1.41 and 1.52 eV)
at high temperatures.
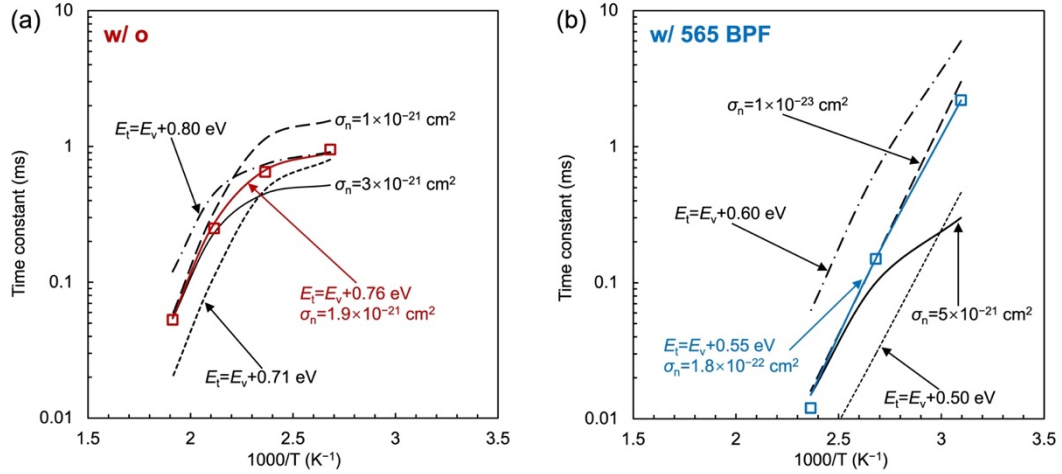
Fig. 4. Temperature dependence of time constants of (a) w/ o and (b) w/ 565 BPF curves from TR-PL measurements. Symbols and lines represent experimental and calculated results, respectively. Solid coloured lines correspond to calculation using $E_T = E_v + 0.76$ eV and $\sigma_n^T = 1.9 \times 10^{-21}$ cm^2 for (a) w/ o BPF and using $E_T = E_v + 0.55$ eV and $\sigma_n^T = 1.8 \times 10^{-22}$ cm^2 for (b) w/ 565 BPF. Other lines are obtained by calculations using different E_T and σ_n^T.

5.4 Numerical analysis

The PL spectra only include the observed peaks, and since the signals detectable by TR-PL also correspond to luminescence in each wavelength range, there is a correlation between wavelength and time constant. Therefore, through numerical analysis, the estimation of the energy levels of defects influencing at least the emission probability can be determined. To explain the temperature-dependent time constants, we calculated the TR-PL decay curves based on the rate equations for carrier trapping and emission [9,10,22,23]. Similar to our previous study on GaN [12], the decay was generally caused by the trapping of charge minority carriers at deep levels. The CeO$_2$ sample was assumed to be an n-type semiconductor. At low temperatures, excess free majority carriers recombine with trapped minority residing at deep energy levels. When the majority carrier capture cross-section at the minority traps is exceedingly small, the transition time constant becomes protracted. As the temperature increases, trapped minority carriers are emitted from the traps, subsequently recombining with surplus-

free majority carriers at the recombination centers. [13]. Consequently, an increase in temperature reduces the time constant associated with the slow decay.

Based on this mechanism with an assumption of n-type conductivity, we calculated the temporal changes in the concentrations of free electrons n and free holes p using the following equations [22]:

$$\frac{dn}{dt} = -\sigma_n^T v_{th} n(N_T - n_T) + e_n^T n_T - \sigma_n^R v_{th} n(N_R - n_R) + e_n^R n_R \tag{1}$$

and

$$\frac{dp}{dt} = -\sigma_p^T v_{th} p n_T + e_p^T (N_T - n_T) - \sigma_p^R v_{th} p n_R + e_p^R (N_R - n_R), \tag{2}$$

where σ_n^T (σ_p^T) is the capture cross-section of the traps for electrons (holes), v_{th} is the thermal velocity of the carriers, N_T (N_R) is the concentration of the traps (the recombination centers), n_T (n_R) is the concentration of electrons at the traps (the recombination centers), and e_n^T (e_p^T) is the emission coefficient for the electrons (holes) at the traps. Superscript "R" of σ and e indicates the values for the recombination centers. The relationship between e_n^T and σ_p^T can be expressed as [13]

$$e_n^T = \sigma_n^T v_{th} N_c \exp\left(\frac{-(E_c - E_T)}{kT}\right), \tag{3}$$

where N_c is the effective density of states in the conduction band, E_c is the edge of the conduction band, and E_T is the trap energy level. A similar relationship exists between e_p^T and σ_p^T and also for the recombination centers. To calculate the N_c and the effective density of states in the valance band, N_v, which is adopted in the relationship between e_p^T and σ_p^T, we employed the effective masses of electrons and holes as $0.4m_0$, respectively [24–27], where m_0 is the rest electron mass. Similarly, the rate equations for the traps and recombination centers are

$$\frac{dn_{\mathrm{T}}}{dt} = \sigma_n^{\mathrm{T}} v_{\mathrm{th}} n (N_{\mathrm{T}} - n_{\mathrm{T}}) - e_n^{\mathrm{T}} n_{\mathrm{T}} - \sigma_n^{\mathrm{T}} v_{\mathrm{th}} p n_{\mathrm{T}} + e_n^{\mathrm{T}} (N_{\mathrm{T}} - n_{\mathrm{T}}) \tag{4}$$

and

$$\frac{dn_{\mathrm{R}}}{dt} = \sigma_n^{\mathrm{R}} v_{\mathrm{th}} n (N_{\mathrm{R}} - n_{\mathrm{R}}) - e_n^{\mathrm{R}} n_{\mathrm{R}} - \sigma_n^{\mathrm{R}} v_{\mathrm{th}} p n_{\mathrm{R}} + e_n^{\mathrm{R}} (N_{\mathrm{R}} - n_{\mathrm{R}}), \tag{5}$$

respectively. Even though band-to-band emission is not observed, we calculated the initial decay as a product of n and p as $I_{\mathrm{initial}} \propto n \cdot p$. We then mainly focused on reproducing the following component corresponding to the carrier recombination at the trap level producing PL. Therefore, we calculated the signal of $I_{\mathrm{PL}} \propto n \cdot (N_{\mathrm{T}} - n_{\mathrm{T}})$ both w/ o and w/ 565 BPF. The full-spectrum TR-PL signals were obtained using $I_{\mathrm{full}} = I_{\mathrm{initial}} + I_{\mathrm{PL}}$ and the time constants defined similarly to the experimental values were extracted.

We considered CeO₂ to have the majority carrier concentration at equilibrium carrier concentration, which was assumed to be 3×10^{16} cm^{-3} in this experiment considering the case of β-Ga₂O₃, ZnO, and SnO single crystals [28–31] whose equilibrium carrier concentrations are generally of the order of 10^{16}–10^{18} cm^{-3}. Although, considering the unique band structure of CeO₂, the conductivity type and majority concentration may be different from this assumption, this value only affects the value of the capture cross-section. Therefore, we can estimate the location of the energy levels of the defects even with the assumption. The recombination centers were assumed to be in the middle of the bandgap gap [10], $E_{\mathrm{R}} = E_{\mathrm{v}} + 1.6$ eV. Concurrently, we set the capture cross-section of the recombination centre for electrons and holes as $\sigma_n^{\mathrm{R}} = \sigma_p^{\mathrm{R}} = 10^{-15}$ cm^2, which is a typical value [10,12,13]. The concentration of the recombination center, N_{R}, was set at 4×10^{15} cm^{-3} to reproduce the similar order of the time constants for decay curves with time constants shorter than 1 μs. We set the concentration of the traps, N_{T}, to be 3×10^{14} cm^{-3}, which is one order of magnitude lower than N_{R} and σ_p^{T} to be the same typical value of 10^{-15} cm^2 for recombination center, whereas σ_n^{T} was taken as a variable parameter. The energy level of the traps was also variable both w/ o 565 BPF

(HT$_{\text{infrared}}$) and w/ 565 BPF (HT$_{\text{visible}}$). The parameters are listed in Table 1.

Table 1. Parameters used for calculation of rate equations.

	Hole traps (HT$_{\text{infrared}}$ / HT$_{\text{visible}}$)	Recombination centres
Energy level (E_t)	Variable	$E_v + 1.6$ eV
Electron capture cross-section (σ_n)	Variable	10^{-15} cm^2
Hole capture cross-section (σ_p)	10^{-15} cm^2	10^{-15} cm^2
Concentration	3×10^{14} cm^{-3}	4.2×10^{15} cm^{-3}

To estimate the trap parameters, the experimental and calculated time constants were compared, and the results are shown in Fig. 3. For the w/ o BPF 565 case [Fig. 3(a)], the time constant depends on E_T above the temperature at which the time constant decreases rapidly. The best fit of E_T with the experimental results is achieved at $E_T = E_v + 0.76$ eV. Concurrently, below ~430 K, the time constant depends on σ_n^T, and the calculated value is 1.9×10^{-21} cm^2 for HT$_{\text{infrared}}$. However, σ_n^T linearly depends on the assumed N_T, and thus, we only claim that σ_n^T will be of the order of 10^{-21} cm^2. For the w/ 565 BPF case [Fig. 3(b)], different from the w/ o 565 BPF trend, the time constant monotonically decreases. Moreover, $E_T = E_v + 0.55$ eV, which is shallower than the that of the w/ o 565 BPF case. Furthermore, $\sigma_n^T = 1.8 \times 10^{-22}$ cm^2, which is one order of magnitude smaller than that of the w/ o 565 BPF case and shows the best fit for HT$_{\text{visible}}$. We calculated based on the n-type conductivity, however, the materials can be p-type. Therefore, the estimated E_T is located at 0.76 eV from the conduction or valance band, the capture cross-section of the majority carrier, σ^T, is the order of 10^{-21}

cm^2 for HT$_{infrared}$. Also, E_T is 0.55 eV from the conduction or valance band, σ^T is the order of 10^{-22} cm^2 for HT$_{visible}$. For both HT$_{infrared}$ and HT$_{visible}$, the estimated σ^T values are less than 10^{-21} cm^2, and such small capture cross-sections indicate that the traps have large lattice distortion depending on their charge states [32,33].

HT$_{infrared}$ shows deeper E_T and larger σ^T than those for HT$_{visible}$. This result is consistent with the persistent peak intensities in the infrared region in the PL spectra (Fig. 1) at high temperatures. The energies of the PL peaks are 2.01 and 2.16 eV for the visible light region and 1.41 and 1.52 eV for the infrared region. Considering the band gap of CeO$_2$, the transition energies of the electrons or holes from the conduction or valence band are 1.04−2.16 eV and 1.41−1.79 eV for the visible light and infrared regions, respectively. However, the estimated energy levels from the temperature dependence of the decays are 0.76 eV and 0.55 eV from the conduction or valance band for HT$_{visible}$ and HT$_{infrared}$, respectively, which are smaller than those estimated from the PL spectra. The energy difference between the optical and thermal transitions can be attributed to the Franck–Condon (FC) shift [34–36]. The large FC shifts indicate that the defects depend on the lattice coordinates of the charge states, which is consistent with their small σ_n as also observed for III–V semiconductors, particularly GaAs, InP, and GaN [37–42]. These results help understand the structures of the defects that contribute to carrier recombination in CeO$_2$. Moreover, for the defect structure, the ratio of O/Ce is around 2.2, confirming the O-rich for our sample, therefore, the possibility of the presence of Ce vacancy and O interstitial is significantly high, and Ce^{3+}-related defects, such as oxygen vacancy, is not present. Huang's group reported the native defect structure and energy levels of CeO$_2$ using the first-principles calculation, the energy level of Ce vacancy and O interstitial is 0.55 eV below the conduction band and 0.80 eV above the valance band [43], respectively, which are comparable to our calculated results.

5.5 Conclusion

In summary, we observed the charge carrier recombination of an undoped CeO$_2$

single crystal with (100) crystal face by TR-PL and μ-PCD measurements. The presence of defects in the material was confirmed by the observation of several peaks at the corresponding energy levels in the PL spectra. From the injected photon density independence of the decay curves under all excitation conditions, that Auger recombination was inferred to have a negligible effect on this sample. The TR-PL decay curves displayed PL in both visible light and infrared regions. To quantitatively analyze the properties of each defect level, we observed these decay curves separately using a 565 nm BPF and then reproduced the time constants based on the model considering trapping and emission through the hole traps HT$_{infrared}$ (w/ o 565 BPF) and HT$_{visible}$ (w/ 565 BPF). The estimated E_T is located at 0.76 eV from the conduction or valance band and σ^T is of the order 10^{-21} cm^2 for HT$_{infrared}$, and E_T is located at 0.55 eV from the conduction or valance band and σ^T is of the order 10^{-22} cm^2 for HT$_{visible}$ indicated different degrees of impact on carrier recombination corresponding to the PL spectra. Generally, these defects negatively affect photocatalytic applications. Although the CeO$_2$ single crystal has better crystalline quality than other crystal types, it is characterized by many defects. Therefore, defect control of this material should be considered during the synthesis of all crystal types to improve and develop photocatalytic applications.

References

[1] E. Kusmierek, *Catalysts*, **10**, 1435 (2020).

[2] D.P.H. Tran, M.-T. Pham, X.-T. Bui, Y.-F. Wang, and S.-J. You, *Solar Energy*, **240**, 443–466 (2022).

[3] Q. Li, L. Song, Z. Liang, M. Sun, T. Wu, B. Huang, F. Luo, Y. Du, and C.-H. Yan, *Adv Energy and Sustain Res*, **2**, 2000063 (2021).

[4] H.Y. Kim, H.M. Lee, and G. Henkelman, *J. Am. Chem. Soc.*, **134**, 1560–1570 (2012).

[5] C. Yang, Y. Lu, L. Zhang, Z. Kong, T. Yang, L. Tao, Y. Zou, and S. Wang, *Small Structures*, **2**, 2100058 (2021).

[6] G. Forghieri, D. Zanardo, E. Ghedini, F. Menegazzo, A. Giordana, G. Cerrato, A. Di Michele, G. Cruciani, and M. Signoretto, *Catalysts*, **11**, 1209 (2021).

[7] M. Kato, H. Najima, and T. Ozawa, *J. Electrochem. Soc.*, **166**, H468–H472 (2019).

[8] S.M.A. Durrani, M.F. Al-Kuhaili, and I.A. Bakhtiari, *Sensors and Actuators B: Chemical*, **134**, 934–939 (2008).

[9] N. Lobo, T. Kawane, G.J. Matt, A. Osvet, S. Shrestha, L. Ievgen, C.J. Brabec, A. Kanak, P. Fochuk, and M. Kato, *Jpn. J. Appl. Phys.*, **61**, 125503 (2022).

[10] M. Kato, T. Ozawa, and Y. Ichikawa, *J. Phys. D: Appl. Phys.*, **54**, 345106 (2021).

[11] K. Tanaka, K. Nagaya, and M. Kato, *Jpn. J. Appl. Phys.*, **62**, SC1017 (2023).

[12] M. Kato, T. Maeda, K. Ito, K. Tomita, T. Narita, and T. Kachi, *Jpn. J. Appl. Phys.*, **61**, 078004 (2022).

[13] M. Kato, T. Asada, T. Maeda, K. Ito, K. Tomita, T. Narita, and T. Kachi, *Journal of Applied Physics*, **129**, 115701 (2021).

[14] T. Asada, Y. Ichikawa, and M. Kato, *JoVE*, 59007 (2019).

[15] K. Tanaka and M. Kato, *AIP Advances*, **13**, 085220 (2023).

[16] E. Zhang and M. Kato, *J. Phys. D: Appl. Phys.*, **56**, 025103 (2023).

[17] M. Kato, Z. Xinchi, K. Kohama, S. Fukaya, and M. Ichimura, *Journal of Applied Physics*, **127**, 195702 (2020).

[18] S. Mochizuki and F. Fujishiro, *Physica Status Solidi (b)*, **246**, 2320–2328 (2009).

[19] V. Seminko, P. Maksimchuk, I. Bespalova, A. Masalov, O. Viagin, E. Okrushko, N. Kononets, and Y. Malyukin, *Phys. Status Solidi B*, **254**, 1600488 (2017).

[20] J. Calvache-Muñoz, F.A. Prado, L. Tirado, L.C. Daza-Gomez, G. Cuervo-Ochoa, H.L. Calambas, and J.E. Rodríguez-Páez, *J Inorg Organomet Polym*, **29**, 813–826 (2019).

[21] M. Kato and Y. Kato, *Chemical Physics Letters*, **805**, 139955 (2022).

[22] M. Ichimura, *Solid-State Electronics*, **50**, 1761–1766 (2006).

[23] T. Okuda, H. Miyake, T. Kimoto, and J. Suda, *Jpn. J. Appl. Phys.*, **52**, 010202 (2013).

[24] L. Truffault, M. Magnani, P. Hammer, C.V. Santilli, and S.H. Pulcinelli, *Colloids and Surfaces A: Physicochemical and Engineering Aspects*, **471**, 73–80 (2015).

[25] F. Zhang, Q. Jin, and S.-W. Chan, *Journal of Applied Physics*, **95**, 4319–4326 (2004).

[26] Z. Wang, Z. Quan, and J. Lin, *Inorg. Chem.*, **46**, 5237–5242 (2007).

[27] L. Nadjia, E. Abdelkader, B. Naceur, and B. Ahmed, *Journal of Rare Earths*, **36**, 575–587 (2018).

[28] S. Roy, A. Bhattacharyya, and S. Krishnamoorthy, *IEEE Trans. Electron Devices*, **67**, 4842–4848 (2020).

[29] P. Kumari, U. Punia, D. Sharma, A. Srivastava, and S.K. Srivastava, *Silicon*, **15**, 2099–2112 (2023).

[30] E. Dumons, L.P. Tran-Huu-Hue, and G. Poulin-Vittrant, *Advcd Theory and Sims*, 2300369 (2023).

[31] M. Minohara, A. Samizo, N. Kikuchi, K.K. Bando, Y. Yoshida, and Y. Aiura, *J. Phys. Chem. C*, **124**, 1755–1760 (2020).

[32] S. Gupta, E. Simoen, R. Loo, Y. Shimura, C. Porret, F. Gencarelli, K. Paredis, H. Bender, J. Lauwaert, H. Vrielinck, and M. Heyns, *Applied Physics Letters*, **113**, 022102 (2018).

[33] M. Bruzzi, F. Gabelloni, N. Calisi, S. Caporali, and A. Vinattieri, *Nanomaterials*, **9**, 177 (2019).

[34] H. Zhang, L. Shi, X. Yang, Y. Zhao, K. Xu, and L. Wang, *Advanced Optical Materials*, **5**, 1700404 (2017).

[35] A. Alkauskas, C.E. Dreyer, J.L. Lyons, and C.G. Van De Walle, *Phys. Rev. B*, **93**, 201304 (2016).

[36] M.A. Reshchikov, *Physica Status Solidi (a)*, **220**, 2200402 (2023).

[37] M.C. Arikan, C.B. Hatch, and B.K. Ridley, *J. Phys. C: Solid State Phys.*, **13**, 635–650 (1980).

[38] E.H. Tyler, M. Jaros, and C.M. Penchina, *Applied Physics Letters*, **31**, 208–210 (1977).

[39] A. Dadgar, R. Engelhardt, M. Kuttler, and D. Bimberg, *Phys. Rev. B*, **56**, 10241–

10248 (1997).

[40] D. Bayaa, G. Bastide, M. Rouzeyre, and A. Sibille, *Solid State Communications*, **51**, 359–363 (1984).

[41] A. Armstrong, D. Green, A.R. Arehart, U.K. Mishra, J.S. Speck, and S.A. Ringel, *MRS Proc.*, **831**, E5.7 (2004).

[42] M.A. Reshchikov, D.O. Demchenko, M. Vorobiov, O. Andrieiev, B. McEwen, F. Shahedipour-Sandvik, K. Sierakowski, P. Jaroszynski, and M. Bockowski, *Phys. Rev. B*, **106**, 035206 (2022).

[43] B. Huang, R. Gillen, and J. Robertson, *J. Phys. Chem. C*, **118**, 24248–24256 (2014).

Chapter 6

Conclusion and future work outlook

6.1 Conclusion

In this study, charge carrier dynamics and photoelectrochemical properties of photocatalyst single crystals for solar-to-hydrogen energy conversion was characterized. The conclusions are summarized as follows:

For TiO_2, 3C-SiC single crystals, and the tandem structure, the pH dependence and irradiation light intensity dependence of photocurrents were characterized. The dependence shows that the performance of the tandem structure is limited by the photocurrent from the TiO_2 photoanode. The maximum ABPE from the tandem structure was 0.74% with no additional bias applied. Gas generation confirmed that the tandem structure can be used for solar water splitting. The durability of the tandem structure was tested for up to 100 days. Therefore, this tandem structure is a promising system.

For $BiVO_4$ single crystals with the (001) and (100) crystal faces, the carrier lifetimes were characterized using the TR-PL and μ-PCD methods. For the (001) face, the carrier lifetime was dominated by the surface and SRH recombination, while for the (100) face, the carrier lifetime was dominated only by SRH recombination. Our estimated S and τ_{bulk} show a larger S and a longer τ_{bulk} corresponding to the smaller N_r for the sample with the (001) face compared to those for the sample with the (100) face. We believe that these quantitative S which indicates a difference in the density of the surface states owing to the atomic configurations and τ_{bulk} which indicates the slight difference in bulk quality values will be helpful for improving the design and energy conversion efficiency of $BiVO_4$ photocatalyst.

For the unpolished and polished TiO_2 and $SrTiO_3$ single crystals, our observations

72

revealed that µ-PCD curves exhibited a clear slow decay, indicating the presence of traps on the unpolished faces. The insensitivity of the polished face to temperature can be attributed to deep recombination centers in SRH recombination. Furthermore, the opposite temperature dependences observed for the unpolished TiO_2 and $SrTiO_3$ faces indicate that carrier recombination is induced by different mechanisms in the recombination centers of these two materials. The XPS analysis revealed a high concentration of oxygen vacancies in the unpolished $SrTiO_3$ face, indicating the presence of oxygen defects or hydroxyl. The TEM images confirm the presence of dislocations in the unpolished faces of both materials. These dislocations created minority carrier traps in the unpolished faces, inducing the slow decay observed in the measurements. In addition, a higher photocurrent was observed in the unpolished faces than in the polished faces for both materials. Considering the significantly rougher surface, which increases the contact area with the electrolyte and enhances the light confinement effect, and the apparent increase in carrier lifetime caused by the traps in the unpolished face, it was expected that the photocurrent in the unpolished faces would be higher than that in the polished faces. However, the unpolished face did not have a positive effect on PEC activity. These contrasting results clearly indicate that dislocations have a detrimental impact on the PEC activity, even in the case of TiO_2 and $SrTiO_3$, which are considered to be the most typical photocatalysts for water splitting. Therefore, it is essential to utilize a surface without dislocations to improve the performance of PEC water splitting. These findings will significantly contribute to the development of more efficient processes for photocatalysis.

For the undoped CeO_2 single crystal, the charge carrier recombination on (100) crystal face was characterized by TR-PL and µ-PCD measurements. The observation of several peaks at the corresponding energy levels in the PL spectra confirmed the presence of defects in the material. From the injected photon density independent decay curves under all excitation conditions, Auger recombination was negligible in this sample. The TR-PL decay curves displayed PL in both visible light and infrared regions. To quantitatively analyze the properties of each defect level, we observed these decay

curves separately using a 565 nm BPF and then reproduced the time constants based on the rate equation model considering trapping and emission through the hole traps $HT_{infrared}$ (w/ o 565 BPF) and $HT_{visible}$ (w/ 565 BPF). The estimated $E_T = E_v + 0.76$ eV and σ_n of the order 10^{-21} cm^2 for $HT_{infrared}$ and $E_T = E_v + 0.55$ eV and σ_n of the order 10^{-22} cm^2 for $HT_{visible}$ indicated different degrees of impact on carrier recombination corresponding to the PL spectra. Generally, these defects negatively affect photocatalytic applications. Although the CeO$_2$ single crystal has better crystalline quality than other crystal types, it is characterized by many defects. Therefore, defect control of this material should be considered during the synthesis of all crystal types to improve and develop photocatalytic applications.

6.2. Future work outlook

In the tandem structure combined with TiO$_2$ and 3C-SiC single crystals, both TiO$_2$ and 3C-SiC electrodes show excellent performance in photochemical water splitting. However, the performance of the tandem structure was limited by TiO$_2$ photoanode according to the similarity resulting in the pH and light intensity dependence. If any other materials with high performance and durability can be found or the performance of the TiO$_2$ can be improved by various methods, we believe this promising tandem structure will be a great contribution in PEC water splitting.

The dominant carrier recombination is different in different crystal faces. For the monoclinic BiVO$_4$ single crystal, the density of the surface states owing to the atomic configurations is different between (001) and (100) crystal faces. Generally, the PEC reaction occurs at the interface between the material and the solution (surface of the photocatalyst). Moreover, the carrier recombination can influence the energy conversion efficiency. Therefore, the carrier recombination at the material surface becomes important. In improving the design of BiVO$_4$, we have to notice the influence of the density of the surface states owing to the crystal surfaces and the bulk crystalline quality.

For unpolished TiO_2 and $SrTiO_3$, the longer carrier lifetime owing to the dislocation defects results in a smaller photocurrent compared with the polished samples. This contrasting result indicates that dislocations have a negative impact on the PEC performance, even in the case of TiO_2 and $SrTiO_3$. Even for powders or nanoscale particles, material preparation processes that do not induce dislocations are required to achieve efficient photocatalytic performance. One approach is suggested to soften the surface of the sample through an excellent polishing process, which helps improve the crystalline quality.

The multiple defects are present by observing the photoluminescence and carrier recombination in the CeO_2 single crystal. Each parameter for the defect level is reproduced. Since the single crystal has many defects, defect control should be paid attention even to the synthesis of various types of CeO_2. We believe the parameter and discussion will contribute to defect engineering not only in CeO_2 but also in other photocatalysts.

In the field of hydrogen production from photolyzed water, more and more materials are being developed, and while considering the improvement of energy conversion efficiency, we should also pay attention to the control of surface and internal defects of the material itself and the durability and stability of the material so that it can be widely used in the future.

Published journal papers

1. **Endong Zhang**, Zhenhang Liu, and Masashi Kato, Durable and efficient photoelectrochemical water splitting using TiO_2 and 3C-SiC single crystals in a tandem structure, *Solar Energy Materials & Solar Cells*, 230 (2021) 111260

2. **Endong Zhang** and Masashi Kato, Surface recombination velocities for the (100) and (001) crystal faces of bismuth vanadate single crystals, *Journal of Physics D: Applied Physics*, 56 (2022) 025103 (5pp)

3. **Endong Zhang**, Mingxin Zhang, and Masashi Kato, Effect of dislocations on carrier recombination and photoelectrochemical activity in polished and unpolished TiO_2 and $SrTiO_3$ crystals, *Journal of Applied Physics*, (upcoming publication).

4. **Endong Zhang**, Christoph J. Brabec, and Masashi Kato, Analysis of defects dominating carrier recombination in CeO_2 single crystal for photocatalytic applications, *Physica Status Solidi – Rapid Research Letters*, (undergoing review).

Presentation

1. **Endong Zhang,** Christoph J. Brabec, and Masashi Kato: "Analysis of defects dominating carrier recombination in CeO_2 single crystal for photocatalytic applications" *Solid State Devices and Materials*, 2023.09.07 (Nagoya, Japan).